Delft University of Technology

Parameters for the collapse of turbulence in the stratified plane Couette flow

van Hooijdonk, Ivo G.S.; Clercx, Herman J.H.; Ansorge, Cedrick; Moene, Arnold F.; van de Wiel, Bas J.H.

Citation (APA)
van Hooijdonk, I. G. S., Clercx, H. J. H., Ansorge, C., Moene, A. F., & van de Wiel, B. J. H. (2018). Parameters for the collapse of turbulence in the stratified plane Couette flow. *Journal of the Atmospheric Sciences*, *75*(9), 3211-3231. https://doi.org/10.1175/JAS-D-17-0335.1

Important note
To cite this publication, please use the final published version (if applicable).
Please check the document version above.

Parameters for the Collapse of Turbulence in the Stratified Plane Couette Flow

IVO G. S. VAN HOOIJDONK AND HERMAN J. H. CLERCX

Fluid Dynamics Laboratory, and J. M. Burgerscentrum, Eindhoven University of Technology, Eindhoven, Netherlands

CEDRICK ANSORGE

Institute for Geophysics and Meteorology, University of Cologne, Cologne, Germany

ARNOLD F. MOENE

Meteorology and Air Quality Group, Wageningen University and Research, Wageningen, Netherlands

BAS J. H. VAN DE WIEL

Faculty of Civil Engineering and Geosciences, and Remote Sensing, Delft University of Technology, Delft, Netherlands

ABSTRACT

We perform direct numerical simulation of the Couette flow as a model for the stable boundary layer. The flow evolution is investigated for combinations of the (bulk) Reynolds number and the imposed surface buoyancy flux. First, we establish what the similarities and differences are between applying a fixed buoyancy difference (Dirichlet) and a fixed buoyancy flux (Neumann) as boundary conditions. Moreover, two distinct parameters were recently proposed for the turbulent-to-laminar transition: the Reynolds number based on the Obukhov length and the "shear capacity," a velocity-scale ratio based on the buoyancy flux maximum. We study how these parameters relate to each other and to the atmospheric boundary layer. The results show that in a weakly stratified equilibrium state, the flow statistics are virtually the same between the different types of boundary conditions. However, at stronger stratification and, more generally, in nonequilibrium conditions, the flow statistics do depend on the type of boundary condition imposed. In the case of Neumann boundary conditions, a clear sensitivity to the initial stratification strength is observed because of the existence of multiple equilibriums, while for Dirichlet boundary conditions, only one statistically steady turbulent equilibrium exists for a particular set of boundary conditions. As in previous studies, we find that when the imposed surface flux is larger than the maximum buoyancy flux, no turbulent steady state occurs. Analytical investigation and simulation data indicate that this maximum buoyancy flux converges for increasing Reynolds numbers, which suggests a possible extrapolation to the atmospheric case.

1. Introduction

To reduce the complexity of studying the stably stratified atmospheric boundary layer (SBL), we often resort to idealized, conceptual models (André and Mahrt 1982; McNider et al. 1995; Wilson and Venayagamoorthy 2015; van Heerwaarden and Mellado 2016; van de Wiel et al. 2017; Fedorovich et al. 2017). A particularly useful tool with respect to idealized flow configurations is direct numerical simulation (DNS; Moin and Mahesh 1998; Marlatt et al. 2012; Fritts et al. 2016) since it does not require any parameterization of turbulence. Among other limitations, a major drawback of employing DNS is that it cannot resolve flows at atmospheric Reynolds numbers (the scale separation between the largest and smallest scales of turbulence, defined in section 2). As such, it is not always clear how the results extend to the atmospheric case. In this study, we aim to understand how previous advances on the collapse of turbulence based on canonical flow configurations relate to each other. Additionally, we discuss their applicability to the real SBL.

Traditionally, the transition in the SBL was associated with a characteristic value of the Obukhov parameter z/L (with z the height above the surface and L the Obukhov length; Monin 1970) or a Richardson number. Recently, doubt was cast on the suitability of these parameters to mark a transition of the global character of the SBL from weakly stable (WSBL) to very stable (VSBL) (Grachev et al. 2013; van Hooijdonk et al. 2015; Monahan et al. 2015]). As an alternative, van Hooijdonk et al. (2015) used the existence of a maximum in the sensible heat flux transport in the SBL (Taylor 1971; Malhi 1995; van de Wiel et al. 2007) to introduce a new dimensionless ratio coined the "shear capacity." This ratio indicates whether or not the wind speed is strong enough to generate a turbulent heat flux that compensates the radiative energy loss of low-heat-capacity surfaces. Using field observations, van Hooijdonk et al. (2015) and Monahan et al. (2015) showed that this parameter broadly separates the VSBL from the WSBL. In a DNS of a Couette flow, van Hooijdonk et al. (2017b) showed that turbulence collapses when this ratio is less than a critical value.

Several recent studies showed interesting results using DNS of boundary layer flows over a smooth wall with respect to the transition from a turbulent flow to an intermittent or laminar flow. It appears that this transition occurs when stratification suppresses the near-wall generation of turbulence, which was characterized by the so-called Obukhov–Reynolds number (Flores and Riley 2011). This parameter indicates the ratio between the Obukhov length L (Monin 1970) and the smallest turbulent length scale, the wall unit ν/u_τ (e.g., Kim et al. 1987). Several studies show that for a large range of Reynolds numbers $[O(10^3)–O(10^5)]$ and for different configurations the transition to intermittent or laminar occurs when this ratio is $O(100)$ (Flores and Riley 2011; Deusebio et al. 2015; Ansorge and Mellado 2016; Zhou et al. 2017). This transition was explicitly associated with the transition from a WSBL to a VSBL as defined by Mahrt et al. (1998), although it is unclear how this transition parameter translates to rough surfaces. Moreover, a truly laminar flow is unlikely to occur in the real SBL, as indicated by observations (Mauritsen et al. 2007) and the occurrence of intermittency in numerical simulations at supercritical stability (Ansorge and Mellado 2014), that is, where traditional stability analysis predicts laminarization.

Both the shear capacity and the Obukhov–Reynolds number indicate a transition in strongly stratified idealized flows. One possibility is that the two parameters are essentially the same. However, the shear capacity is expressed using bulk variables (wind speed, height), while the Obukhov–Reynolds number is expressed in wall variables (friction velocity, surface heat flux). Therefore, it is unlikely that both parameters have the same physical meaning. Consequently, we may ask the following questions: How do these parameters relate to each other? What is their respective physical relevance? And what is their relevance for the SBL?

To answer these questions, we perform DNS of the Couette flow with a fixed heat (or, more generally, buoyancy) flux (Neumann) boundary conditions (BCs) imposed at the top and bottom walls. We opt for DNS instead of large-eddy simulation (LES; e.g., as in Armenio and Sarkar 2002) since the closure paradigms of LES are violated in strongly stratified, intermittent flows. We investigate the flow at several combinations of the (bulk) Reynolds number and the shear capacity, which are the external parameters for this configuration. Thereby, this investigation directly extends the results of van Hooijdonk et al. (2017b). The results of these simulations are then discussed in relation to previous studies of related configurations using DNS (with cooling turned on instantly at $t = 0$), such as the Ekman flow (Ansorge and Mellado 2016; Gohari and Sarkar 2017), the plane channel flow (Flores and Riley 2011; García-Villalba and del Álamo 2011), and the Couette flow with a fixed bulk temperature difference (Deusebio et al. 2015).

Between these configurations, there is a clear hierarchy, with the Ekman flow being the most realistic, but also the most complex, configuration. Here, we opt for investigating the Couette flow for three reasons: First, symmetry of the problem allows us to combine the DNS results with analytical considerations. Second, as argued in van de Wiel et al. (2012a) and van Hooijdonk et al. (2017b), this configuration captures several essential features of the real SBL in the first few hours after sunset, particularly in relation to the WSBL–VSBL transition. Third, the collapse of turbulence (i.e., laminarization that is permanent or local in time and/or space) due to a stable density gradient appears to be controlled by the same mechanism in different wall-bounded flow configurations (Scotti and White 2016; Zhou et al. 2017).

Generality of the collapse mechanism also exists between different temperature BCs (Flores and Riley 2011; Mellado 2012; Deusebio et al. 2015), but there is no clear hierarchy in terms of realism between imposing a constant heat flux or isothermal walls. The most realistic choice would evidently be the inclusion of a soil model (e.g., as in Smirnova et al. 1997; Steeneveld et al. 2006). However, this requires additional model choices and may not be feasible computationally. Therefore, idealized surfaces are typically used in conceptual studies (Garg et al. 2000; Ansorge and Mellado 2014). Since the applicability

of different temperature BCs has been debated in several papers (Basu et al. 2008; Gibbs et al. 2015; van de Wiel et al. 2017), a particular question is, What is the relative impact of choosing imposed fluxes (Neumann) or isothermal walls (Dirichlet) as BCs for buoyancy? The advantage of the latter is that it allows for more control over the stratification strength, since the bulk stratification does not dynamically interact with the flow. But in reality, dynamical interactions between the bulk buoyancy gradient and turbulent mixing may be very important, for example, for predictions of the nighttime surface temperature (Fernando and Weil 2010; Holtslag et al. 2013).

To study the impact of the temperature BCs, we also apply DNS. Unlike one-dimensional eddy viscosity [Reynolds-averaged Navier–Stokes (RANS)] models of similar systems (van de Wiel et al. 2007; Holdsworth et al. 2016; van de Wiel et al. 2017), DNS does not rely on the assumption that the flow is horizontally homogeneous or that turbulent fluxes are in instantaneous equilibrium with the mean flow. Both assumptions become invalid for a fast-evolving strongly stratified flow. As such, a DNS may be used to reevaluate RANS-based predictions of the dynamical behavior.

In summary, this paper aims to identify 1) how the critical value of the shear capacity (van Hooijdonk et al. 2017b) relates to the transition marked by the Obukhov–Reynolds number and 2) what the differences and similarities are, both in terms of temporal evolution and the statistically steady state, between applying a fixed flux (Neumann) or a fixed difference (Dirichlet) as temperature BC for the Couette flow.

Following the presentation of specific methods, parameters, and simulation strategy in section 2, we extend the findings of van Hooijdonk et al. (2017b) by discussion of the flow characteristics as function of the shear capacity (section 3a). Boundary conditions (flux driven or isothermal) are analyzed by comparison of the steady-state statistics as well as the dynamical behavior (section 3b). For the Dirichlet cases, we use the DNS of Deusebio et al. (2015) for interpretation, and a quantitative comparison is made with additional simulations. We further investigate the relation between the critical value of the shear capacity, which is associated with maximization of the turbulent buoyancy flux (van Hooijdonk et al. 2015, 2017b), with the Reynolds number (section 3c) as well as the Obukhov–Reynolds number (section 3d). The gradient Richardson number at the centerline of the flow is shown to be associated with a maximum buoyancy flux in section 3e, while the bulk Richardson number does not seem to govern the collapse adequately. This presentation is finalized by the discussion (section 4) and summarizing conclusions (section 5).

2. Theory and methods

a. Model setup and dimensionless numbers

The Couette flow consists of a horizontally infinite domain (mimicked by periodic BCs), which is vertically symmetric around the centerline at $z = h$, and it is vertically bounded by the walls at $z = 0$ and $z = 2h$. These walls are moving in opposite directions with velocity $\pm U_0$. The horizontal motion of the walls generates a shear layer in between the walls. As argued in van de Wiel et al. (2012b), around sunset, a height exists around which the wind velocity is close to constant. We consider the bottom half of the Couette flow a model for the SBL during this period [e.g., see the sketches in Fig. 1 of Zhou et al. (2017)]. Furthermore, a constant wall flux is being used as a model for the relatively constant net radiative energy loss of an isolating surface under clear-sky conditions in relatively dry environments. On Antarctica, such conditions are approximated quite closely (Vignon et al. 2017), while in general, this approximation is rather crude.

For this setup, the governing flow equations for an incompressible fluid under the Boussinesq approximation are

$$\frac{\partial u_i}{\partial x_i} = 0, \tag{1a}$$

$$\frac{\partial u_i}{\partial t} = -u_j \frac{\partial u_i}{\partial x_j} - \frac{1}{\rho_0} \frac{\partial p}{\partial x_i} - b\delta_{i3} + \nu \frac{\partial^2 u_i}{\partial x_j^2}, \tag{1b}$$

$$\frac{\partial b}{\partial t} = -u_j \frac{\partial b}{\partial x_j} + \kappa_b \frac{\partial^2 b}{\partial x_j^2}, \tag{1c}$$

for conservation of mass, momentum, and heat, respectively (Einstein summation convention applies). In these equations, u_i represents the velocity components $\{u_1 = u, u_2 = v, u_3 = w\}$ of a fluid parcel at time t and position $\{x_1 = x, x_2 = y, x_3 = z\}$, δ_{ij} is the Kronecker delta ($\delta_{ij} = 1$ when $i = j$ and 0 otherwise), p is the pressure, ρ_0 the reference density, ν is the kinematic viscosity, and κ_b is the molecular diffusion of buoyancy. For generality, we define the buoyancy $b = gT/T_0$, with T the temperature deviation with respect to an arbitrary reference temperature $T_0 \gg T$ and g the acceleration by gravity.

For this setup we define the (bulk) Reynolds number as $\mathrm{Re} = U_0 h/\nu$, which varies between 1000 and 6200, at least three to four orders of magnitude lower than for the real SBL. The molecular Prandtl number ($\mathrm{Pr} = \nu/\kappa_b$) is kept constant at 1 for simplicity. Recent findings by Zhou et al. (2017) indeed suggested that there is only a very minor impact of varying between $\mathrm{Pr} = 1$ and $\mathrm{Pr} = 0.7$ (the value for air). The definition of

the external stratification parameter depends on the buoyancy BCs.

For velocity, no-slip BCs are imposed; that is, $u = \pm U_0$ and $v = w = 0$ at the walls. Horizontally, a periodic domain is being used. For buoyancy, we apply Neumann (flux) BCs in most cases; that is,

$$\partial_z b_{\text{wall}} = q_w/\kappa_b, \qquad (2)$$

with $-q_w$ the imposed buoyancy flux through the walls. The external control parameter is then the shear capacity of the Couette flow (van Hooijdonk et al. 2017b), which is defined as

$$\text{SC}_C = U_0/(hq_w)^{1/3}. \qquad (3)$$

Physically, SC_C represents a ratio of velocity scales: U_0 is the wall velocity, and $(hq_w)^{1/3}$ is proportional to the velocity at the maximum total (diffusive plus turbulent) buoyancy flux $\phi_{b,\text{max}}$ equals q_w, which occurs at value $\text{SC}_C = \text{SC}_C^{\text{crit}}$. Thus, $\text{SC}_C^{\text{crit}}$ indicates whether or not the turbulent flow can sustain the buoyancy flux needed to match the BC. In the Couette flow, SC_C provides a definite answer (at least for a given Re; see van Hooijdonk et al. 2017b) about the final state of the flow being turbulent or laminar. For the plane channel flow, this may be different. In that configuration, turbulence may collapse temporarily when q_w is too large (Flores and Riley 2011). Subsequently, turbulence recovers because of reacceleration of the flow (Businger 1973; Donda et al. 2015). Donda et al. (2015) showed that when a different initial velocity profile (i.e., one for which shear is initially larger than in a logarithmic profile) was used, the flow may remain turbulent at all times.

The bulk Richardson number Ri_b is defined as

$$\text{Ri}_b = \frac{h\Delta b}{U_0^2}, \qquad (4)$$

with $\Delta b = 0.5[b(z = 2h) - b(z = 0)]$. In the flux-driven case (with SC_C as an external parameter), Ri_b is an internal parameter representing the bulk stratification. In case Dirichlet BCs for buoyancy are being applied, it is $\Delta b = B_0$, with $\pm B_0$ the imposed buoyancy at the walls.

While Re is the external parameter setting the scale separation, it is not the exact turbulence scale separation of the flow. The latter is related to the—a priori unknown—wall friction. The actual scale separation between the domain-scale h and the smallest-scale ν/u_τ is described by the friction Reynolds number $\text{Re}_\tau = u_\tau h/\nu$, with $u_\tau^2 = \nu[\partial_z u](z = 0)$. This parameter characterizes the near-wall behavior of the flow. Taking into account the limiting effect of stability on the largest scales, Flores and Riley (2011) introduced an

additional scale separation, the Obukhov–Reynolds number, defined as

$$\text{Re}_L = \frac{Lu_\tau}{\nu}, \qquad (5)$$

with $L = u_\tau^3/(\kappa q_w)$ the Obukhov length and κ the von Kármán constant. The Obukhov length is interpreted as the height at which buoyancy becomes more limiting for turbulence than the wall distance. For $L \lesssim O(h)$, the Obukhov–Reynolds number indicates the ratio of the size of the largest turbulent motions of $O(L)$ compared to the smallest turbulent motion of $O(\nu/u_\tau)$. Flores and Riley (2011) suggested that turbulence cannot survive when this ratio is less than $O(100)$. The scale separation Re_L is based on similar arguments as the buoyancy Reynolds number (Smyth and Moum 2000; Billant and Chomaz 2001; Brethouwer et al. 2007), defined as

$$\text{Re}_b = \left(\frac{l_O}{\eta}\right)^{4/3} = \frac{\varepsilon_{\text{tke}}}{\nu N^2}, \qquad (6)$$

in which l_O, the Ozmidov scale, defines the length scale below which turbulence is assumed to be isotropic; η is the Kolmogorov length scale; ε_{tke} is the dissipation of the turbulent kinetic energy (TKE); and $N = \sqrt{\partial_z b}$ is the Brunt–Väisälä frequency (also called buoyancy frequency). It was suggested that this parameter provides a better characterization of strongly stratified flows than a Richardson number (e.g., Shih et al. 2005; Bartello and Tobias 2013). The parameters Re_L and Re_b are related as

$$\text{Re}_b \simeq \kappa \text{Re}_L, \qquad (7)$$

by assuming the scaling relations $\varepsilon_{\text{tke}} \sim u_\tau^3/l$ and $N^2 \sim q_w/(u_\tau l)$. In this relation, l is the mixing length (assumed equal for momentum and buoyancy). The DNS results by Zhou et al. (2017) show good agreement with (7) for a wide range of Re, Pr, and Ri_b. Since both ε_{tke} and N are height dependent, the numerical values of Re_b may depend on the averaging volume. Conversely, Re_L takes a single value, since it is defined based on wall variables only. Therefore, Re_L is likely more relevant for characterizing the state of the SBL, and hence, we focus our discussion on this parameter.

b. Numerical method

Equations (1a)–(1c) are solved using the DNS algorithm of van Heerwaarden et al. (2017; https://github.com/microhh/microhh). The algorithm is used with a fractional-step (Kim and Moin 1985) third-order Runge–Kutta scheme for time integration and a CFL number of 1. The spatial discretization is of second order, and it is

based on finite differences, with uniformly distributed grid points. The code also allows for fourth-order accuracy, but since no significant differences were observed when, for example, evaluating the dissipation profiles, the second-order spatial discretization is used to limit computational cost.

Profiles of statistical quantities (e.g., budget terms of the Reynolds stresses) were stored at each time unit h/U_0. To this end, the flow variables are Reynolds decomposed into horizontally averaged fields $U_i = \langle u_i \rangle$, $B = \langle b \rangle$ (where $\langle \cdot \rangle$ indicates averaging in the horizontal plane) and fluctuating fields $u_i' = u_i - U_i$, $b' = b - B$. Unless stated otherwise, these quantities are presented in inertial units, that is, normalized using U_0 and h.

The resolution is chosen such that under neutral stratification it is in the range 2.5–$5.4\nu/u_t$ horizontally and 0.7–$1.4\nu/u_t$ vertically. A list of the resolution for each simulation is presented in appendix A (Table A1). We verified that the budget terms of the TKE agree very closely between different Reynolds numbers and with previous numerical results under neutrally stratified conditions (appendix B). Moreover, we verified the height independence of the total fluxes of momentum and buoyancy.

c. Case setup

A specific goal is to determine the critical value of SC_C below which turbulence cannot be sustained at each Re. We investigate the flow evolution for decreasing values of SC_C at six values of Re. For each Re, the Couette flow is initialized with a randomly perturbed logarithmic profile. Equations (1) are then solved for 250–$300 h/U_0$ until a turbulent, statistically steady state is obtained. The final state of the neutral initialization is then used as the initial condition for the stratified cases with the corresponding Reynolds number. When $SC_C \approx 22$–24, a significantly longer time was required to reach a steady state. Therefore, to limit computational cost, two cases are started from fully turbulent fields instead of starting from the neutrally stratified initial state (see Table 1).

When possible, the time-averaged steady-state values of Re_τ, Re_L, and Ri_b were obtained. These values are also listed in Table 1 for comparison. The relative standard deviation of each quantity is approximately 1% or less (measured by the standard deviation during the averaging period). If a simulation does not acquire a statistically steady state within the simulated time (marked with an asterisk in Table 1), the final value of these dimensionless ratios is listed.

To investigate the effect of the initial and the BCs, additional simulations are performed (Table 2). To compare the steady-state statistics, the steady-state Ri_b is measured for several cases in which Neumann BCs

are used. This value for Ri_b is then used as a control parameter in a new simulation (labeled RxxRxxx), in which Dirichlet BCs are used. The difference between applying Dirichlet or Neumann BCs is the quantities that are fixed at the top and bottom boundary, summarized as follows:

- Dirichlet BC: b_{wall} fixed, $\partial_z b_{wall}$ free;
- Neumann BC: b_{wall} free, $\partial_z b_{wall}$ fixed.

Another set of simulations is initialized with a strongly stratified state of the flow (labeled RxxVSxxx). For these cases, Neumann BCs are imposed such that $SC_C > SC_C^{crit}$, as listed in Table 2, to investigate the evolution for different initial conditions.

3. Results

a. Flow characteristics versus the shear capacity

In this section, we investigate the evolution of the flow at different SC_C, as well as the steady state of the flow when $SC_C < SC_C^{crit}$. Particularly, we investigate if the results at Re = 3500 are consistent with previous studies. A comparison between different Re is made in subsequent sections.

Figure 1a shows the velocity profile for each value of SC_C at Re = 3500. For $SC_C \geq 23.7$ (based on the present simulations), the profiles correspond to a statistically steady state. For these cases, the Obukhov length is still larger than the domain half height (e.g., at $SC_C = 23.7$, $h/L \approx 0.32$), which indicates a weak influence of the density gradient. When $SC_C < 23.7$, the flow is not in a steady state at the end of the simulation. For these cases, a tendency toward a linear profile (the laminar steady state) is observed, with the exception of case R35S231 (i.e., Re = 3500, $SC_C = 23.1$), for which it is unclear if a turbulent steady state can be maintained. In agreement with Deusebio et al. (2015; using Pr = 0.7), we find that the buoyancy profiles (Fig. 1b) are similar in shape to the velocity profile at a Prandtl number of order unity.

Zhou et al. (2017) suggested that the gradient Richardson number $Ri = \langle \partial_z b \rangle / [\langle \partial_z u \rangle]^2$ cannot exceed 0.2 in a turbulent Couette flow. Indeed, we find that Ri nowhere exceeds 0.195 for Re = 6200 (with even lower values for lower Re). Although this corresponds closely to the limit predicted by Zhou et al. (2017), we cannot exclude the possibility that Ri exceeds 0.2 at even larger Reynolds numbers based on the present results.

Within the atmospheric context, it is well known that turbulence may exist at $Ri \gg 0.2$ (and also $h/L \gg 0.32$). As such, caution needs to be taken when extrapolating current results to the real atmosphere. In the atmospheric

TABLE 1. Overview of all simulations with Neumann BCs. Single asterisks indicate that no steady state was reached during the simulation. The double asterisks indicate initialization from a fully turbulent, stably stratified field obtained during the run listed directly above (i.e., with a slightly larger value of SC_C). The columns read from left to right: the run label (based on the values of Re and SC_C), Re, SC_C, the steady-state period (or total run time) in inertial and in turbulent time units, and the steady (or final)-state values of Re_τ, Re_L, and Ri_b.

Run	Re	SC_C	$\frac{th}{U_0}$	$\frac{th}{u_\tau}$	Re_τ	Re_L	Ri_b
$L_x, L_y, L_z = 48h, 24h, 2h$			$n_x, n_y, n_z = 1056, 528, 144$				
R10	1000	∞	350	23	66	∞	0
R10S271	1000	27.1	150	9	60	637	0.026
R10S252	1000	25.2	150	8	56	380	0.042
R10S244*	1000	24.4	650	33	51	228	0.043
R10S237*	1000	23.7	450	19	43	110	0.055
$L_x, L_y, L_z = 48h, 24h, 2h$			$n_x, n_y, n_z = 1344, 672, 192$				
R16	1600	∞	1200	74	98	∞	0
R16S317	1600	31.7	600	35	94	1530	0.009
R16S252	1600	25.2	600	33	87	500	0.020
R16S244	1600	24.4	400	21	83	406	0.027
R16S237*	1600	23.7	2500	110	64	132	0.052
R16S231*	1600	23.1	400	15	60	95	0.047
R16S225*	1600	22.5	400	13	52	53	0.060
R16S220*	1600	22.0	400	12	46	29	0.075
$L_x, L_y, L_z = 60h, 24h, 2h$			$n_x, n_y, n_z = 1920, 864, 216$				
R25	2500	∞	678	39	145	∞	0
R25S317	2500	31.7	500	28	138	1855	0.010
R25S271	2500	27.1	100	5	135	1070	0.020
R25S237	2500	23.7	700	33	118	418	0.035
R25S231*	2500	23.1	600	23	94	148	0.058
R25S225*	2500	22.5	600	17	69	40	0.084
R25S220*	2500	22.0	600	14	59	200	0.110
$L_x, L_y, L_z = 60h, 24h, 2h$			$n_x, n_y, n_z = 2400, 1056, 272$				
R35S	3500	∞	675	38	195	∞	0
R35S317	3500	31.7	600	32	184	2188	0.011
R35S271	3500	27.1	300	15	176	1130	0.019
R35S237	3500	23.7	573	26	159	500	0.037
R35S231*	3500	23.1	800	34	146	318	0.047
R35S225*	3500	22.5	600	19	111	100	0.071
R35S220*	3500	22.0	600	14	78	22	0.118
R35S215*	3500	21.5	600	13	73	16	0.142
$L_x, L_y, L_z = 60h, 20h, 2h$			$n_x, n_y, n_z = 3024, 1080, 396$				
R45	4500	∞	350	19	243	∞	0
R45S317	4500	31.7	197	10	228	1363	0.012
R45S237	4500	23.7	148	7	199	575	0.037
R45S231*	4500	23.1	500	21	187	402	0.046
R45S225*	4500	22.5	650	19	134	98	0.080
R45S220**	4500	22.0	145	4	114	47	0.100
$L_x, L_y, L_z = 60h, 20h, 2h$			$n_x, n_y, n_z = 3600, 1200, 480$				
R62S	6200	∞	350	18	322	∞	0
R62S317	6200	31.7	128	6	300	2745	0.012
R62S237	6200	23.7	200	8	257	608	0.043
R62S231*	6200	23.1	519	20	241	427	0.052
R62S225**	6200	22.5	207	7	223	287	0.065
R62S215*	6200	21.5	500	12	148	49	0.115

TABLE 2. Overview of additionally performed runs with Dirichlet BCs or different initial conditions. The columns are as in Table 1. For runs that are labeled RxxRxxx (based on the values of Re and Ri_b), Ri_b is an input parameter. The domain sizes and number of grid points in each direction are listed for each Re. The runs labeled RxxVSxxx (based on the values of Re and SC_C) are initialized with a strongly stratified state.

Run	Re	SC_C	$\dfrac{th}{U_0}$	$\dfrac{th}{u_\tau}$	Re_τ	Re_L	Ri_b
$L_x, L_y, L_z = 48h, 24h, 2h$			$n_x, n_y, n_z = 1344, 672, 192$				
R16R009	1600	—	200	12	94	1530	0.009
R16R020	1600	—	200	11	87	500	0.020
$L_x, L_y, L_z = 60h, 24h, 2h$			$n_x, n_y, n_z = 1920, 864, 216$				
R25R010	2500	—	175	10	138	1855	0.010
R25R032	2500	—	200	24	118	418	0.020

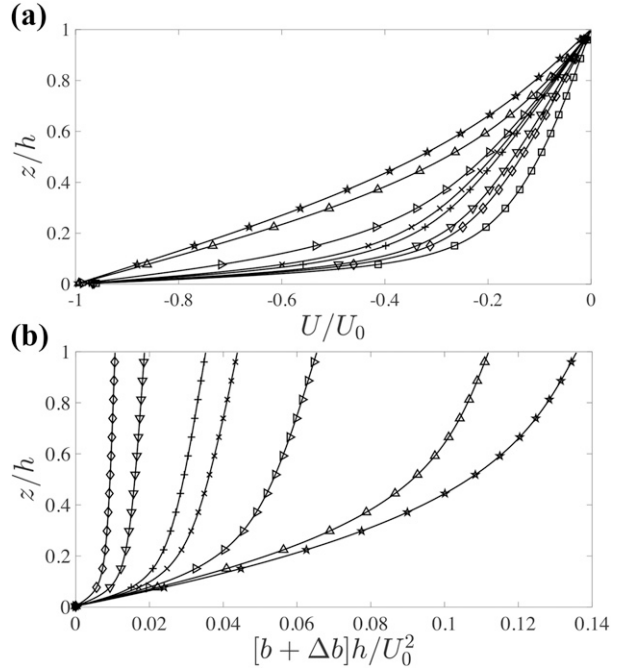| Run	Re	SC_C	$\dfrac{th}{U_0}$	$\dfrac{th}{u_\tau}$	Re_τ	Re_L	Ri_b
$L_x, L_y, L_z = 60h, 24h, 2h$			$n_x, n_y, n_z = 2400, 1056, 272$				
R35R011	3500	—	250	13	184	2188	0.011
R35R037	3500	—	450	20	159	500	0.037
Sensitivity to initial conditions (Neumann BCs)							
R35VS285	3500	28.5	424	17	141	515	0.044
R35VS237	3500	23.7	400	8	69	17	0.124

FIG. 1. (a) Dimensionless velocity and (b) buoyancy profiles between $z = 0$ and $z = h$ for all SC_C at Re = 3500. Each symbol corresponds to a value of SC_C: ∞ ($\square$), 31.7 ($\lozenge$), 27.1 ($\triangledown$), 23.7 ($+$), 23.1 ($\times$), 22.5 ($\triangleright$), 22.0 ($\triangle$), and 21.5 ($\star$).

VSBL, Ri values may greatly exceed the value of 0.2 (Mauritsen et al. 2007; Sun et al. 2015). In particular, processes like clear-air radiative cooling and advection (Derbyshire 1999) and subsidence (Vignon et al. 2017) may result in Ri > 0.2. When extrapolating the present results, one should take into account that these processes are not within our scope.

The bulk Richardson number evidently increases with decreasing SC_C (Fig. 2a). Once $\mathrm{SC}_C < \mathrm{SC}_C^{\mathrm{crit}}$ is in the range of 23.1–23.7, stratification grows significantly in time, and no statistically steady state is reached within the simulated time. The value of Ri_b that corresponds to a laminar steady state (linear profiles) is given by

$$\mathrm{Ri}_b^{\mathrm{lam}} = \mathrm{SC}_C^{-3} \mathrm{Re} \mathrm{Pr} \qquad (8)$$

(e.g., $\mathrm{Ri}_b^{\mathrm{lam}} = 0.35$ for case R35S215). No case was simulated long enough such that values of $\mathrm{Ri}_b \gtrsim \mathrm{Ri}_b^{\mathrm{lam}}/2$ were found. However, the simulation length of some cases was sufficient to observe purely viscous buoyancy transport (albeit not in steady state), that is, coinciding with the prediction $\phi_b h/U_0^3 = \mathrm{Ri}_b/\mathrm{Re}$ (not shown), where ϕ_b is the total buoyancy flux.

All cases resulting in a turbulent steady state ($\mathrm{SC}_C > \mathrm{SC}_C^{\mathrm{crit}}$) have values of $\mathrm{Re}_L \gtrsim 500$ (Fig. 2b; Table 1). Conversely, turbulence collapses once $\mathrm{SC}_C < \mathrm{SC}_C^{\mathrm{crit}}$, as indicated by a runaway decrease of Re_L. The buoyancy
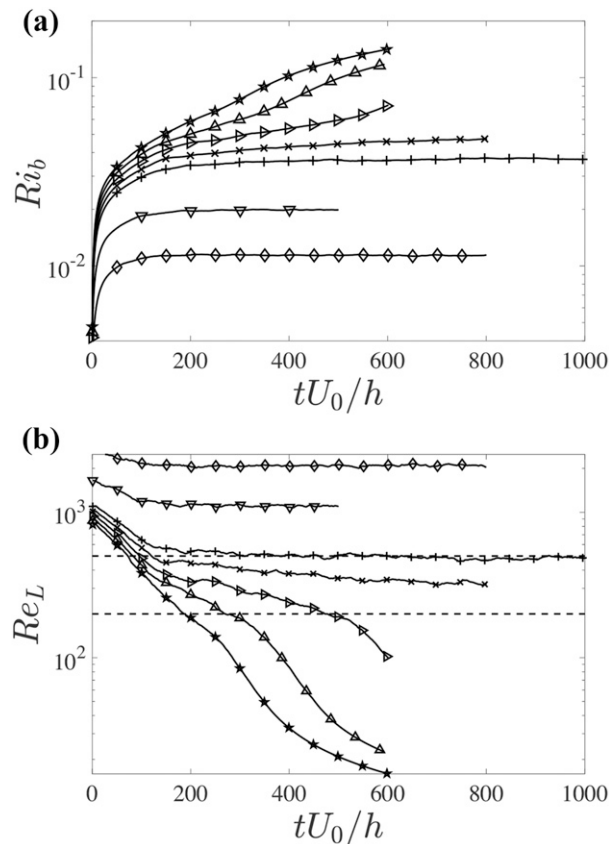
FIG. 2. Evolution of (a) Ri_b and (b) Re_L for all SC_C at Re = 3500. Symbols are as in Fig. 1. Dashed horizontal lines in (b) indicate $Re_L = 200$ and $Re_L = 500$.

FIG. 3. Time series of (a) the buoyancy fluctuations and (b) the turbulent buoyancy flux at $z = h$ for all SC_C at Re = 3500. Symbols are as in Fig. 1.

variance $\langle b'^2 \rangle$ maximizes around $Re_L \approx 150$ (Fig. 3a) while the buoyancy gradient $\langle \partial_z b \rangle$ keeps increasing for higher Re_L. Such a decrease of $\langle b'^2 \rangle$ requires a decrease of $\langle b'w' \rangle_{z=h}$, overcompensating for the growth in $\langle \partial_z b \rangle$ with Re_L. Indeed, as observed in Fig. 3b, the buoyancy flux is maximized already before the collapse occurs, that is, when Re_L is still in the range of 270–350. The sharp decrease of the buoyancy flux around $Re_L \approx 150$ causing a decrease of $\langle b'^2 \rangle$ (despite increasing stratification) hence results from a simultaneous breakdown of both $\langle w'^2 \rangle$ and $\langle b'w' \rangle$. This indication of turbulence breakdown is consistent with the runaway decrease in Re_L for $Re_L \lesssim 150$. As a result of our analysis, we can rule out a transition in the dominant balance of the $\langle b'w' \rangle$ budget: at increasing stratification, the buoyancy destruction term $\langle b'^2 \rangle$ becomes dominating as the buoyancy flux is limited by $\langle \partial_z b \rangle$, that is, the buoyancy flux and variance are not maximized simultaneously. This suggests that the buoyancy flux is not maximizing because of laminarization of the flow. Rather, laminarization occurs because the total buoyancy flux $\phi_b < q_w$ at all times, which inevitably results in a continuous
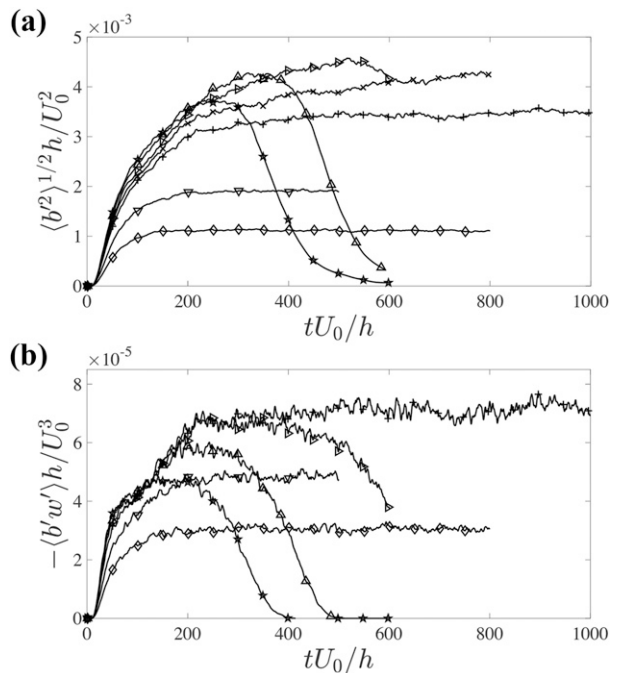
decrease of Re_L (until the laminar limit has been reached). The qualitative changes in the flow when $Re_L \approx 150$ are also visible in Fig. 2a, in which an accelerated increase of Ri_b is observed. The marked transition in the range $Re_L \approx$ 100–200 is consistent with the observations of earlier studies (Flores and Riley 2011).

b. Neumann versus Dirichlet boundary conditions

The similarities of the above results with those by Deusebio et al. (2015) encourage a more detailed comparison of the Couette flow when exposed to either Dirichlet or Neumann BCs. For this purpose, additional simulations have been performed, which are listed in Table 2. Excellent agreement (very closely overlapping lines) was obtained for the production and dissipation profiles between applying the different buoyancy BCs (Fig. 4a). Such agreement was found at Re = 1600 and Re = 2500 and for the other budget terms of the TKE (not shown). In terms of second-order quantities, the effect of the buoyancy BCs is limited to the near-wall region of $\langle b'^2 \rangle$ (Fig. 4b). Further differences mainly manifest themselves in the (higher order) transport and redistribution terms of the $\langle b'w' \rangle$ and $\langle b'^2 \rangle$ budgets, but even then, the differences are most prominent below $z/h \approx 0.15$.

The differences occur because the Dirichlet BC enforces dissipation of any fluctuations of buoyancy at the wall by imposing a strong gradient locally. In the case of
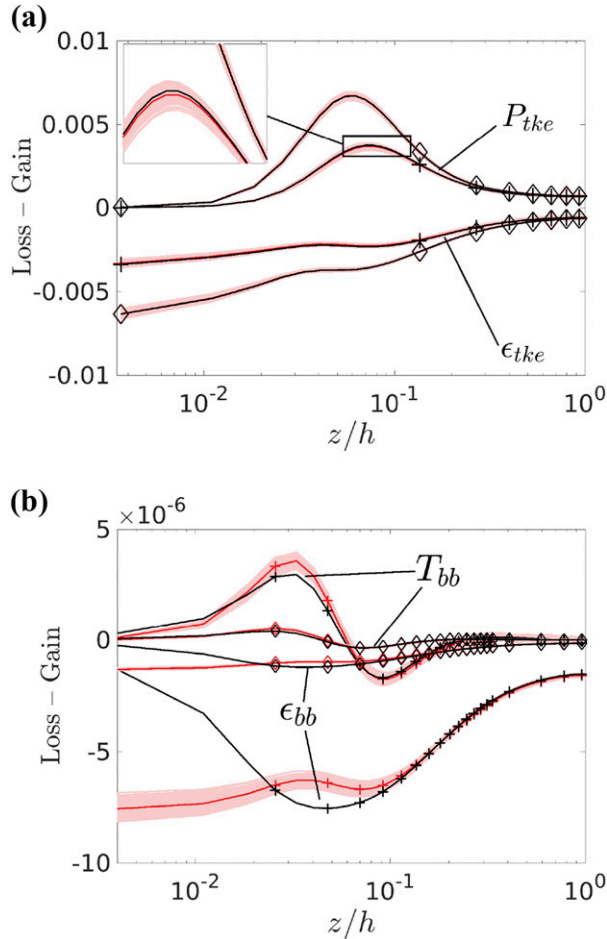
FIG. 4. (a) The time-averaged production P_{tke} and dissipation ε_{tke} profiles of the TKE (as indicated in the figure) and (b) the time-averaged dissipation ε_{bb} and turbulent transport T_{bb} terms of $\langle b'^2 \rangle$. These terms represent the most dominant terms of each budget. The symbols indicate Neumann-BC cases R35S317 (black $\diamond$) and R35S237 (black $+$) and Dirichlet-BC cases R35R011 (red $\diamond$) and R35R037 (red $+$). The thin red lines show the instantaneous profiles to indicate the spread (only for cases R35R011 and R35SR037). The inset in (a) emphasizes the close agreement between BC types.

Neumann BCs, the gradient is fixed, and fluctuations of buoyancy may exist down to $z = 0$. The reasons that these differences do not show up in the TKE budget (i.e., via the buoyancy term in the $\langle w'^2 \rangle$ budget; see Shah and Bou-Zeid 2014) are the no-penetration BC and that the additional $\langle b'^2 \rangle$ in the case of Neumann BCs is being dissipated in the near-wall region (see the peak of ε_{bb} at $z/h \approx 0.04$ in Fig. 4b) instead of reaching the outer layer. The fact that the difference in buoyancy fluctuations does not seem to affect the other flow properties is important because it allows us to compare the first- and second-order (quasi-) steady-state statistics directly, regardless of the buoyancy BCs.

Since the steady states of the flux-driven simulations discussed above are essentially the same as corresponding cases using Dirichlet BCs, we expect that this similarity holds for all stably stratified Couette flow simulations with either Dirichlet or Neumann BCs. However, important differences may exist in terms of dynamic stability. In the Couette flow, this is mainly expressed at strong stratification, when the flow becomes intermittently turbulent. Based on the studies of van de Wiel et al. (2007), Taylor (1971), and Phillips (1972), we may formulate and test the following hypothesis: to the left of the maximum in Fig. 5a, the equilibriums are dynamically stable, while to the right, they are dynamically unstable in case the wall flux is imposed.

The point of departure is the relation between the turbulent buoyancy flux and the bulk Richardson number in a horizontally homogeneous flow. Given Ri_b (Dirichlet BC), a single steady state may be achieved in terms of the buoyancy flux corresponding to exactly one point on the curve in Fig. 5a (Deusebio et al. 2015; Zhou et al. 2017). Conversely, given q_w (Neumann BC), two, one, or zero turbulent equilibriums may exist in terms of Ri_b. If $B_{max}/q_w < 1$ ($SC_C < SC_C^{crit}$), no turbulent solution exists and the flow laminarizes (van Hooijdonk et al. 2017b), where B_{max} is the maximum turbulent flux at $z = h$ and $B_{max} \simeq \phi_{b,max}$, assuming negligible molecular transport at $z = h$. If $B_{max}/q_w > 1$ ($SC_C > SC_C^{crit}$), two turbulent equilibriums exist (points 1 and 2 in Fig. 5a). Suppose the initial system state is given by the lower-left corner of the graph ($Ri_b = 0$). Then the system evolves toward point 1, a dynamically stable equilibrium (indicated by the arrows). Following the RANS-based predictions of van de Wiel et al. (2007), point 2 constitutes a dynamically unstable equilibrium. Thus, depending on the history and forcing of the flow, it will either evolve to point 1 or the flow will collapse toward its laminar equilibrium eventually.

To test this last assertion, the following experiment is conducted: Consider a state with a particular (mean) Ri_b and a (mean) $\langle b'w' \rangle$ corresponding to the right-hand side (rhs) of the maximum in Fig. 5b (black-circled dot), which is used as initial condition for two simulations with new Neumann BCs:

1) $B_{max}/q_w > 1 \wedge \langle b'w' \rangle_{t=0}/q_w < 1$ ($SC_C = 23.7$; solid line in Fig. 5b),
2) $B_{max}/q_w > 1 \wedge \langle b'w' \rangle_{t=0}/q_w > 1$ ($SC_C = 28.5$; dotted line in Fig. 5b).

In both cases, dynamically stable, turbulent equilibriums exist, as found in section 3a. However, in the first case, we expect the system to collapse following the solid arrow. Conversely, in the second case, we expect that a
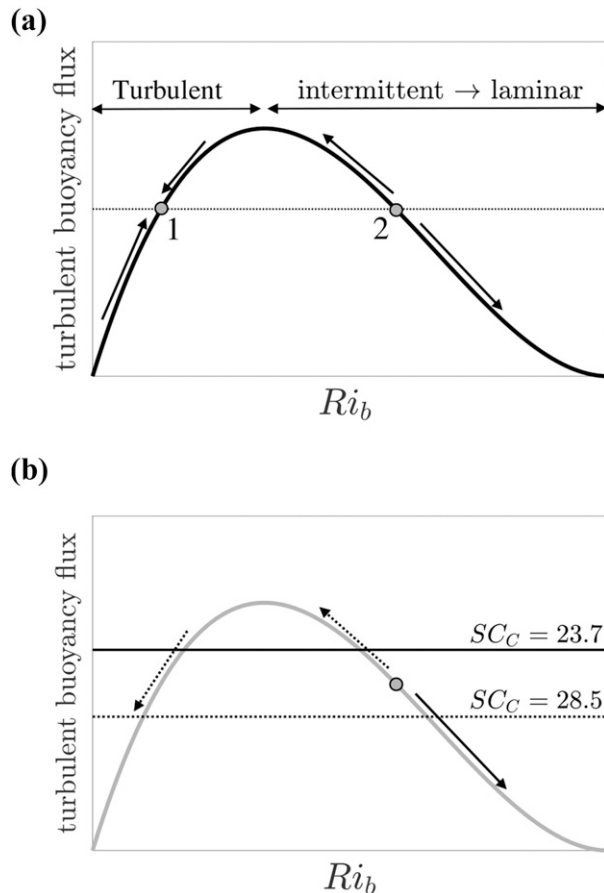
(a)

(b)

FIG. 5. Sketches of the steady-state relation between the turbulent buoyancy flux and the bulk Richardson number. Similar sketches were presented by van Hooijdonk et al. (2015) and Ansorge (2017). The shape of the curve to the right of the maxima is highly uncertain, since the flow is not horizontally homogeneous in this regime. (a) Sketch of the flow character at different stages. The black-circled dots represent conceptual equilibrium states for a specific (absolute value of) imposed wall flux (dashed line). (b) Sketch of the hypothesized evolution for two different imposed wall fluxes (represented by black horizontal lines) when the flow is initialized from a strongly stratified state (black-circled dot). The arrows indicate the hypothesized evolution for the two cases described in the main text: i.e., collapsing (solid) and recovering (dotted).

fully turbulent state is recovered following the dotted arrows.

The first simulation, with $SC_C = 23.7$, indeed shows a collapse (decreasing TKE, increasing Ri_b; see Fig. 6), despite the existence of a turbulent steady state for this value of SC_C (cf. case R35S237 in Fig. 2). For example, the magnitude of the fluctuations decreases three orders of magnitude between Fig. 7a and Fig. 7b. The second simulation shows different behavior. In this case, turbulence almost disappears, and Re_L is temporarily less than 200. However, contrary to the first case, the bulk Richardson number now immediately decreases (Fig. 6),
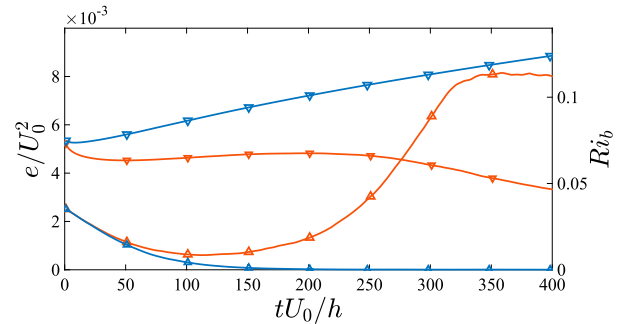

FIG. 6. Time series of the TKE (left axis; symbol $\triangle$) and Ri_b (right axis; symbol $\triangledown$) for two cases with Re = 3500 initialized with a strongly stratified field, i.e., with Ri_b belonging to the rhs of the maximum in Fig. 5. The colors indicate $SC_C = 23.7$ (blue) and $SC_C = 28.5$ (red).

followed by a recovery of turbulence at later times (Fig. 7c). This is also expressed in Re_L, which is close to 500 at the end of the simulation. During the recovery, the buoyancy flux in the center temporarily reaches a value of $\langle b'w' \rangle / q_w \approx 2$ (not shown). This high value is the result of the initial coexistence of recovering turbulence (increasing mixing lengths) and a strong buoyancy gradient, such that each of the newly generated eddies carries extra buoyancy. An interesting observation is that a narrow band along the streamwise direction remains in which turbulence does not recover, at least within the simulated time (Fig. 7c). The most likely explanation is that Ri_b is still quite high for a DNS (~ 0.04) at the end of the run, in combination with the periodic BCs that allow self-reinforcement of the nonturbulent band. These self-reinforcing bands were also observed in literature (Flores and Riley 2011; Deusebio et al. 2015).

The distinct behavior between these simulations pins down a clear dependence on the initial conditions when employing Neumann BCs in a Couette flow. In the Dirichlet case, similar behavior cannot occur, since for given Re and Pr, a unique (in terms of statistical properties) solution exists for each value of Ri_b (Deusebio et al. 2015). Within the atmospheric context, these results are also consistent with the linear stability analysis of van de Wiel et al. (2017). This study coupled the choice of BC to a physically relevant case; that is, Neumann and Dirichlet conditions correspond to fresh and melting snow, respectively.

c. Reynolds number dependence of the critical shear capacity

Several variables exemplify a transition from a fully turbulent steady state to a state of decaying turbulence or laminarization in the range $SC_C \approx 22-24$ (Figs. 8a,b). Moreover, for a given SC_C, the velocity fluctuations
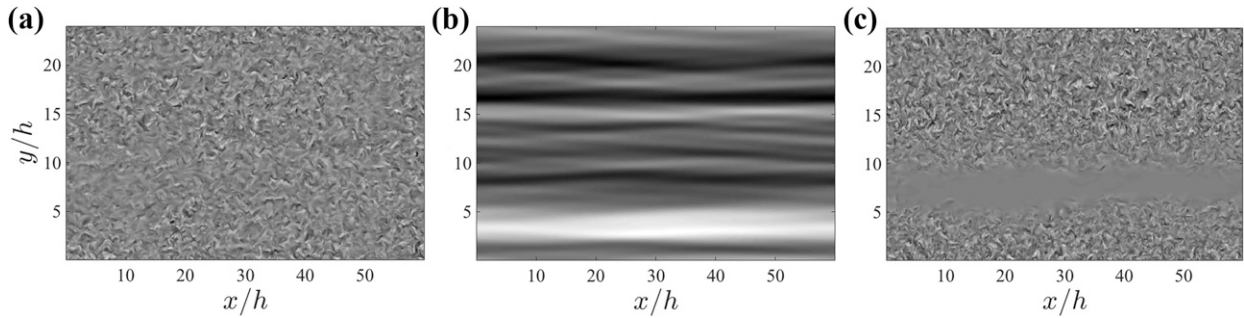
FIG. 7. Instantaneous visualization of horizontal cross sections of the vertical velocity fluctuations at $z = h$ from two cases with Re = 3500 initialized with the same strongly stratified field. (a) The initial field at $t = 0$ for both cases. At $tU_0/h = 400$, (b) the velocity field at when $SC_C = 23.7$ and (c) the velocity field when $SC_C = 28.5$. In (a) and (c), the scale ranges between $w/U_0 = \pm0.05$. In (b), the shades span a range of w that is two orders of magnitude lower than in the other figures.

and the bulk Richardson number are almost independent of Re when $SC_C \gtrsim 24$ and Re > 1600. A closer look at the "critical range" suggests a small dependence of SC_C^{crit} on Re, which is further investigated below.

In most cases, classification as either becoming statistically steady or collapsing is straightforward since, for example, at $SC_C = 31.7$, all cases show statistical steadiness during several hundred h/U_0, while when $SC_C \leq 22.0$, a clear collapse occurs at each Re considered. When SC_C is closer to SC_C^{crit}, a more detailed classification is needed. For this purpose, we analyze two quantities in more detail. First, we investigate the plane-averaged total buoyancy flux in the center of the flow $\langle\phi_b\rangle_{z=h}$. Maximization of $\langle\phi_b\rangle_{z=h}$ (Fig. 9a) followed by a decrease (i.e., the rhs of the maximum in Fig. 5 is reached) indicates that the flow is incapable of matching the BCs (see example cases in Fig. 3).

As a second quantity, we use the normalized buoyancy flux, such that it represents correlation between b' and w' (also at $z = h$), defined as

$$a_{bw} = \frac{|\langle b'w'\rangle|}{(\langle b'^2\rangle\langle w'^2\rangle)^{1/2}}. \qquad (9)$$

This parameter takes an apparently universal value of approximately 0.4–0.45 when the flow is only neutrally or weakly stratified and Re > 1600. This value was also found, for example, in an LES of a plane channel flow (Armenio and Sarkar 2002), in a DNS of a stably stratified Ekman flow (Ansorge and Mellado 2016), and in a DNS of a stably stratified shear flow (Jacobitz et al. 1997). When $SC_C < SC_C^{crit}$, a strong decrease of a_{bw} occurs after some time, which signals a collapse of turbulence (Fig. 9b). The subsequent irregular behavior is a consequence of small values of $\langle b'^2\rangle$ and $\langle w'^2\rangle$. When $SC_C \approx SC_C^{crit}$, we may not obtain a definite answer from our simulations. In these cases (particularly at larger

Re), the flow neither shows signs of a collapse nor of steadiness within the simulated time.

An overview of the classification of all cases (Fig. 10) reveals that the critical shear capacity decreases with increasing Re up to Re = 3500. Beyond this threshold, such clear dependence is not observed. A few cases in a very narrow range around SC_C^{crit} remain nonstationary, that is, they are neither in steady state nor collapsing, which may obscure a possible weak dependence in the relatively high Re range.

d. Interdependency of the Obukhov–Reynolds number and the buoyancy flux

Once $Re_L \lesssim 100$, a_{bw} decreases sharply, indicating decorrelation of the vertical velocity and temperature fluctuations, which is a sign of collapsing turbulence (Fig. 11a, shown for Re $\geq$ 2500 only). Below $Re_L \approx 40$, the behavior is erratic, because $\langle b'^2\rangle$ and $\langle w'^2\rangle$ become small. The overall shape of the curve is independent of Re.

The temporal behavior of individual variables corroborates previous observations of a characteristic value of Re_L marking the transition to intermittent or laminar flow in the Couette, channel and Ekman flow (Deusebio et al. 2015; Flores and Riley 2011; Ansorge 2017), as is indicated by an example case in Fig. 11b. Once Re_L decreases below approximately 200, $\langle w'^2\rangle$ declines gradually in time and more rapidly later, particularly when Re_L is less than 100. Simultaneously, $\langle\partial_z b\rangle_{z=h}$ increases more rapidly, and the evolution of $\langle b'^2\rangle^{1/2}$ changes from increasing to decreasing.

While the onset of intermittency is marked by a narrow range of Re_L, the turbulent buoyancy flux $|\langle b'w'\rangle|$ maximizes in the range $Re_L \approx$ 200–700, depending on Re (Fig. 12a). This maximum precedes, rather than follows, the transition, provided Re is large enough. However, at intermediate Re, the
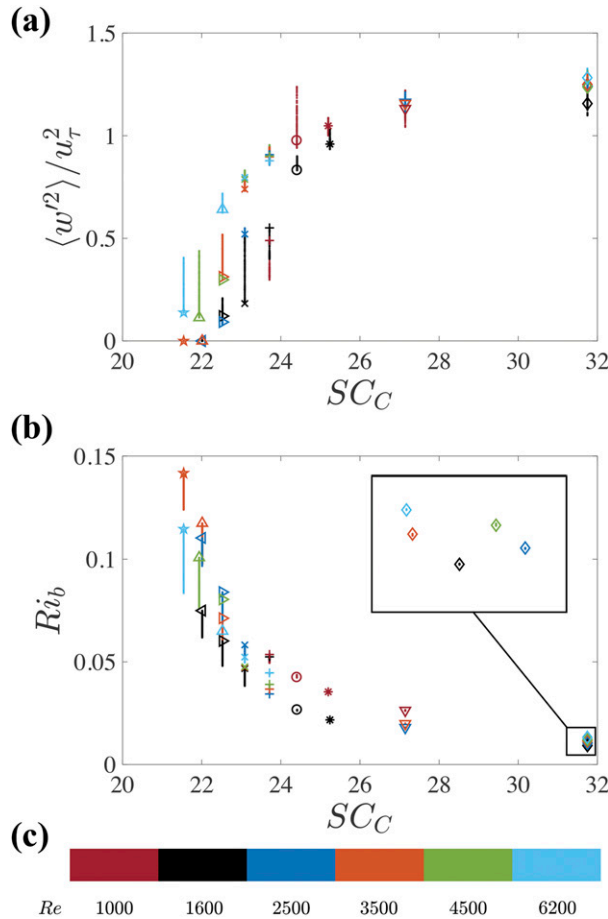
FIG. 8. The final state of (a) $\langle w'^2 \rangle / u_\tau^2$ and (b) Ri_b for each case as a function of SC_C. The trail visualizes the evolution during the final $100h/U_0$ to indicate (non)steadiness of the flow. The inset in (b) shows an enlargement of the overlapping symbols at $SC_C = 31.7$. (c) Each color represents a value of Reshown in (a) and (b). Each symbol corresponds to a value of SC_C: 31.7 ($\diamond$), 27.1 ($\triangledown$), 25.2 (*), 24.4 ($\circ$), 23.7 (+), 23.1 ($\times$), 22.5 ($\triangleright$), 22.0 (Δ), and 21.5 ($\star$).
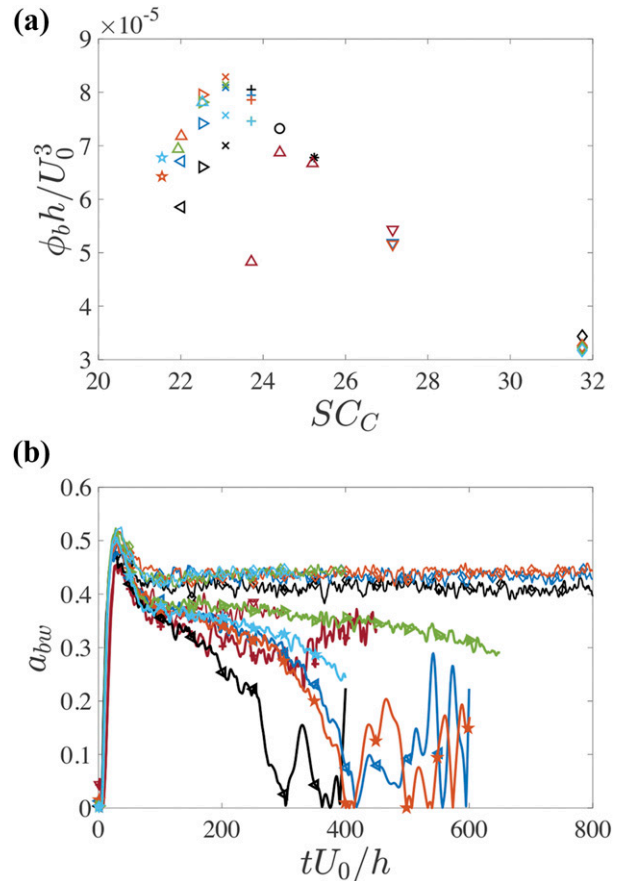
FIG. 9. (a) The maximum instantaneous value of the total buoyancy flux $\langle \phi_b \rangle_{z=h}$ that occurs during the entire simulation. (b) Temporal evolution of the b'–w' correlation [(9)] for a collapsing and a steady-state case for each Reynolds number considered. Colors are as in Fig. 8. Each symbol corresponds to a value of SC_C: 31.7 ($\diamond$), 27.1 ($\triangledown$), 25.2 (*), 24.4 ($\circ$), 23.7 (+), 23.1 ($\times$), 22.5 ($\triangleright$), 22.0 (Δ), and 21.5 ($\star$).

intermittency boundary may be crossed before the buoyancy flux maximizes.

We observe such behavior at Re = 1600 and $SC_C = 23.7$ (case R16S237). This case is run for an extended period until $t = 2500h/U_0$ ($\approx 110h/u_\tau$). During this period, flow rearranged into persistent turbulent/nonturbulent bands (as in Deusebio et al. 2015; not shown). A similar tendency was observed at Re = 1000 (cases R10S244 and R10S237), although the simulation lengths were much shorter for these cases. As such, a statistically steady intermittent state can exist at low Re despite the use of Neumann BCs. This implies that the concepts discussed with respect to Fig. 5 are only valid at sufficiently high Re.

The curves on the (strongly stratified) left-hand side (lhs) of the maximum in Fig. 12a lie much closer

together than on the (weakly stratified) rhs, where the shape of the curves is dependent on Re and SC_C. This indicates that Re_L appropriately characterizes the strongly stratified Couette flow. Conversely, the weakly stratified side shows more scatter, which may be explained by the notion that a turbulent stratified flow requires more than one parameter to characterize the flow under all stability conditions (Shih et al. 2005; Brethouwer et al. 2007). Alternatively, the larger scatter here may be due to the initial transient, since the flow is initialized on the weakly stable side of the maximum (see section 3e).

A pivotal parameter to assess the dynamical stability of the system from its external parameters is the value of the Obukhov–Reynolds number that yields the maximum buoyancy flux. Figure 12b shows that this value increases as a function of Re, which is supported by theoretical analysis of a bulk model. In the limit of
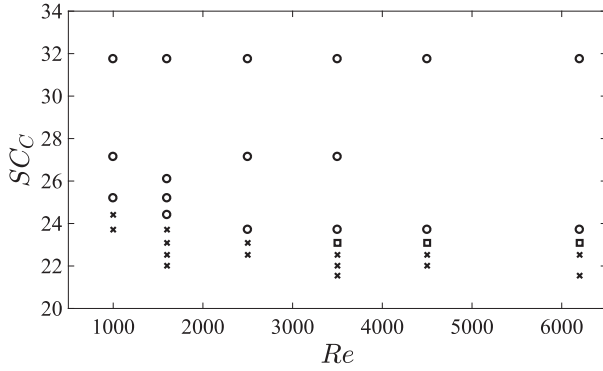
FIG. 10. Overview of all runs in the Re–SC_C plane. The runs are classified by the following symbols: Circles represent cases that are in a turbulent steady state. Crosses show a significant decrease in TKE and a similar increase of Ri_b, which is associated with a collapse. The squares indicate cases that did not become steady within the simulated time but also did not show signs of a collapse of turbulence.

large Re, this analysis yields (see appendix C for a derivation)

$$Re_L \sim \frac{27\alpha}{4\kappa} \frac{Re_\tau}{\ln(Re_\tau)}. \tag{10}$$

Since Re_τ increases with Re, (10) shows that the value Re_L at the maximum buoyancy flux is an increasing function of Re within the limits of these derivations. Additionally, the obtained relation suggests that at low Re, near-wall processes become limiting [i.e., Re_L becomes less than $O(10^2)$] before ϕ_b reaches its maximum value based on the global constraint that scales as U_0^3/h. At larger Re, the buoyancy flux maximizes when $Re_L > O(10^2)$, which marks the onset of positive feedback toward $Re_L \sim O(10^2)$ and thus toward laminarization.

To obtain a quantitative estimate of Re_L when $\phi_b = \phi_{b,max}$, we need to know the functional dependence of Re_τ on Re and Ri_b. For specific Re and Ri_b, the value of Re_τ may be estimated using Monin–Obukhov similarity theory (MOST) extended with an appropriate wall model (e.g., van Driest 1956). Alternatively, the values as listed in Table 1 may be used. This indicates that, indeed, the value of Re_L at the transitional SC_C increases with Re. It also suggests that at the transition point $Re_L > O(10^2)$ when $Re > O(10^3)$, meaning that the presently used Re are only just sufficient to observe the flux maximum resulting from a global constraint. Moreover, (10) suggests that the value of Re_L at the flux maximum increases slowly with increasing Re and that a very large value of Re is required to observe $Re_L \gg O(100)$ at $SC_C = SC_C^{crit}$.
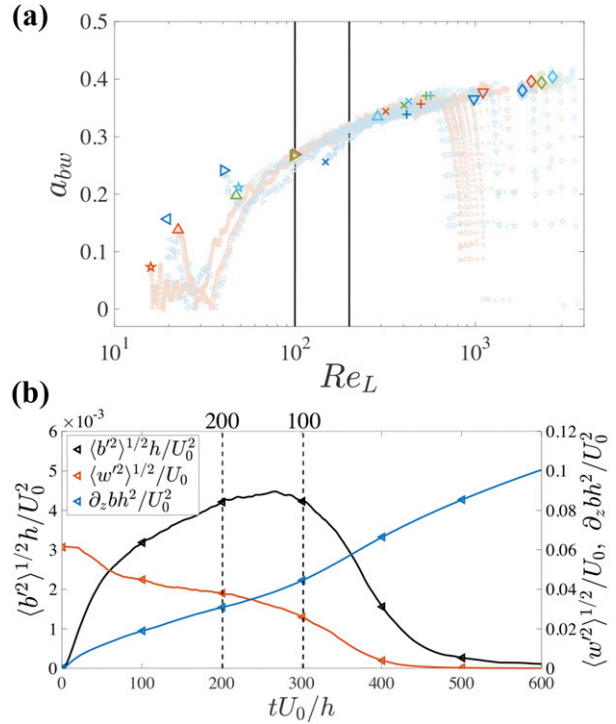

FIG. 11. (a) The correlation between fluctuations of buoyancy and the vertical velocity as function of Re_L. The trail of lighter symbols visualizes the temporal behavior with a thick symbol marking the end point of each simulation. Colors are as in Fig. 8c. Each symbol corresponds to a value of SC_C: 31.7 ($\diamond$), 27.1 (∇), 25.2 (*), 24.4 ($\bigcirc$), 23.7 (+), 23.1 ($\times$), 22.5 ($\triangleright$), 22.0 ($\triangle$), and 21.5 ($\star$). For clarity, the data for Re = 1000 and Re = 1600 are not shown. See appendix B (Fig. B1a) for a comparison with data from an Ekman flow. (b) Time series of the buoyancy fluctuations (black; left axis), the vertical velocity fluctuations (red; right axis), and the buoyancy gradient at $z = h$ (blue; right axis) for Re = 3500 with $SC_C = 21.5$. The vertical lines highlight the time when $Re_L = 200$ and $Re_L = 100$.

e. Richardson number versus buoyancy flux

In this section, we investigate if the occurrence of a maximum turbulent buoyancy flux can be characterized by a Richardson number. The maximum buoyancy fluxes at Re = 1000 (dark red) and Re = 1600 (black) are significantly lower than at larger Re (Fig. 13a). For increasing Re, $\langle b'w' \rangle_{max}$ becomes progressively less sensitive to Re, which is suggesting convergence.

While the value of the maximum flux may become independent of Re, the bulk Richardson number associated with the maximum does not show a similar convergence (at least at the present Re). This appears to contradict MOST-based prediction using a bulk model of a Couette flow with rough walls (van de Wiel et al. 2012b), where the maximum was associated with $Ri_b = 1/(3\alpha)$, with α a fit parameter for the Businger–Dyer flux–profile relations (Businger et al. 1971). Possibly
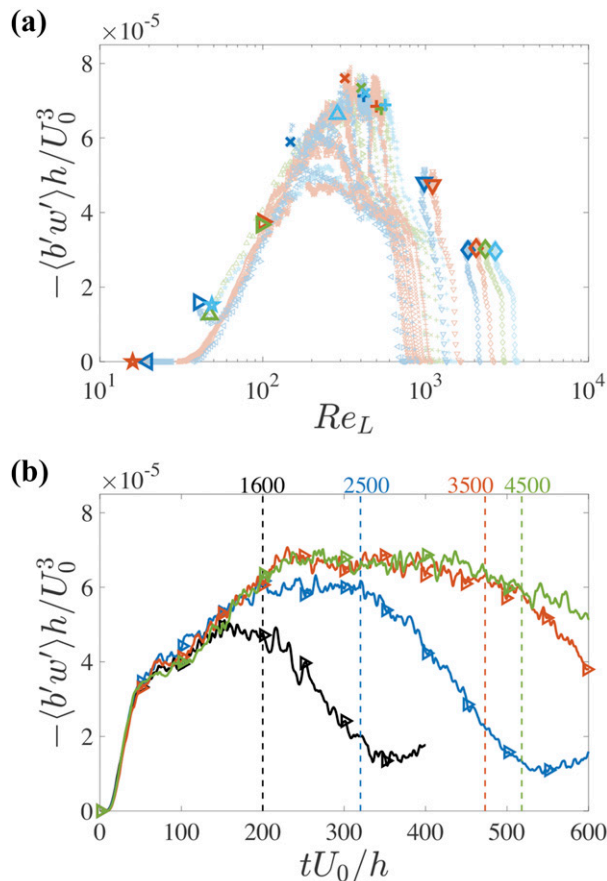
FIG. 12. (a) The buoyancy flux as function of Re_L. The trail of lighter symbols visualizes the temporal behavior, with a thick symbol marking the end point of each simulation. Colors are as in Fig. 8c. Each symbol corresponds to a value of SC_C: 31.7 ($\diamond$), 27.1 ($\triangledown$), 25.2 (*), 24.4 ($\bigcirc$), 23.7 (+), 23.1 ($\times$), 22.5 ($\triangleright$), 22.0 ($\triangle$), and 21.5 ($\star$). (b) Evolution of $\langle b'w' \rangle$ for Re = 1600 (black), 2500 (blue), 3500 (red), and 4500 (green) and $SC_C = 22.5$. Vertical line indicates the time when $Re_L = 200$ for each Reynolds number with the corresponding color.
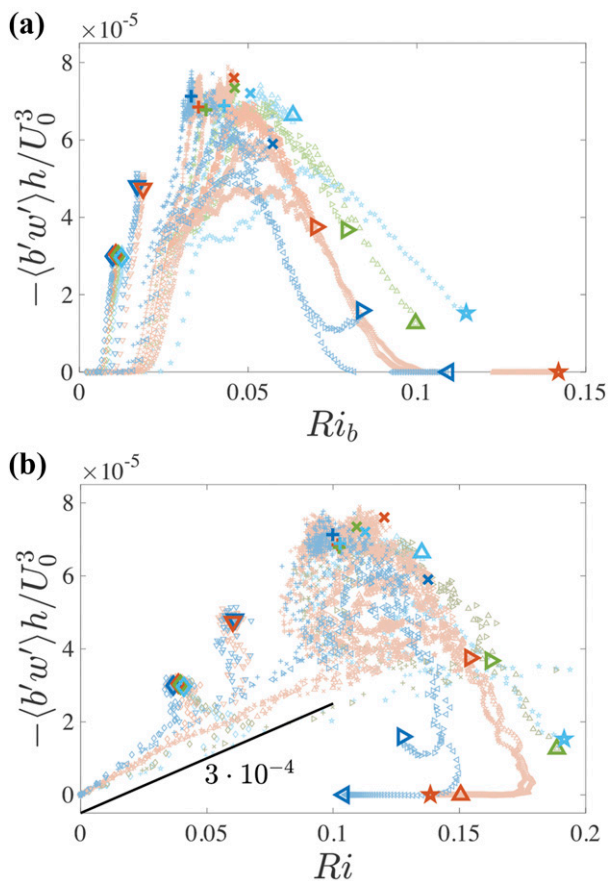
FIG. 13. The mean turbulent buoyancy flux between $z = 0$ and $z = h$ as function of the (a) bulk Richardson number and (b) gradient Richardson number at $z = h$. The trail of lighter symbols visualizes the temporal behavior, with a thick symbol marking the end point of each simulation. Colors are as in Fig. 8c. Each symbol corresponds to a value of SC_C: 31.7 ($\diamond$), 27.1 ($\triangledown$), 25.2 (*), 24.4 ($\bigcirc$), 23.7 (+), 23.1 ($\times$), 22.5 ($\triangleright$), 22.0 ($\triangle$), and 21.5 ($\star$). For clarity, the data for Re = 1000 and Re = 1600 are not shown in (b).

the difference exists because the bulk model neglects the viscous damping in the buffer layer. Additionally, the model considers only one flux–profile relation. Others may show more complex dependency on z_0 (Holdsworth et al. 2016), particularly when z_0 is low (as is the case for smooth DNS wall).

Contrary to Ri_b, the local gradient Richardson number Ri at $z = h$ attains a unique value of $Ri \approx 0.1$ at the maximum, with only a slight increasing tendency for larger Re (Fig. 13b). Particularly on the weakly stratified side of the maximum, the steady-state values (large symbols) in the $[Ri - \langle b'w' \rangle]$ plane form a single curve. This is consistent with the assumption of Phillips (1972) that the buoyancy flux can be expressed in terms of local gradients. Conversely, on the rhs, the data do not collapse, indicating that local gradients are no longer

representative of the local flux. In the limited context of the current low-Re DNS, no specific critical bulk Richardson number could be discerned marking the transition from WSBL to VSBL.

Finally, we observe that for the lowest SC_C, the maximum buoyancy flux is not reached (e.g., when Re = 6200, $SC_C = 21.5$; light-blue star in Fig. 13a). The initial turbulence is damped so strongly that the simulation enters straight into the slow evolution on the strongly stratified side of the maximum buoyancy flux. From a MOST perspective, each value of Ri is associated with a single value of the buoyancy flux (for a specific value of Re) since turbulence is always in instantaneous equilibrium with the mean flow. A consequence is that, within the MOST framework, the flow should trace the same curve in Fig. 13a, irrespective of SC_C

(but not necessarily of Re). Interestingly, the turbulent buoyancy flux at $z = h$ initially follows the line $\langle b'w'\rangle h/U_0^3 \approx 3 \times 10^{-4}\text{Ri}$ for each case (Fig. 13b). However, this line is not close to the equilibrium curve (the virtual line interpolating the thick symbols in Fig. 13b at Ri $\lesssim 0.1$). When $\text{SC}_C > \text{SC}_C^{\text{crit}}$, the equilibrium curve is reached after some time following a line of constant Ri, while the buoyancy flux is still increasing. The fact that we observe all cases following a different curve from the equilibrium curve indicates limited applicability of MOST-based parameterizations for a fast-evolving environment (Nadeau et al. 2011; van Hooijdonk et al. 2017a). When $\text{SC}_C < \text{SC}_C^{\text{crit}}$, the temporal evolution traces a complex line in the Ri–$\langle b'w'\rangle$ plane, which is associated with the onset of intermittent flow.

4. Discussion

Above, we relate the occurrence of a maximum buoyancy flux to a global constraint (expressed by SC_C) and to wall dynamics (expressed by Re_L). Below, the occurrence of this maximum in the present results is discussed in relation to previous studies. Regarding the kind of BC, the equilibrium may depend on the initial turbulent buoyancy flux for Neumann-type BCs, which is consistent with theoretical considerations on the maximum buoyancy flux. Such a dependency is not found for Dirichlet-type BCs. Section 4b elaborates on how this result may be extended to other flow configurations.

a. Parameters for the collapse of turbulence

The existence of a maximum buoyancy flux finds support from theoretical work (Taylor 1971; Phillips 1972; van de Wiel et al. 2007; Caulfield and Kerswell 2001), from field observations in the atmosphere and in the ocean (Posmentier 1977; Malhi 1995; Monahan et al. 2015; van Hooijdonk et al. 2015), and from laboratory experiments (Linden 1979; Holford and Linden 1999). A main point of discussion is how the occurrence of this maximum is properly characterized and whether the buoyancy flux decreases when stratification becomes even stronger.

The present results extend previously obtained insight into the merits of three distinct parameters and into their relation to each other.

- The Obukhov–Reynolds number Re_L is related to the turbulent fraction at strong stability. Consistent with the present results, earlier studies observed relaminarization of the flow in the plane channel flow (Flores and Riley 2011), the Couette flow (Deusebio et al. 2015), and the Ekman flow (Ansorge 2017) once $\text{Re}_L \lesssim 100 - 200$. In the Ekman flow, the turbulent fraction depended on the initial conditions when Re_L was in the range of 200–800.

- The shear capacity SC_C is an external bulk parameter for the Couette flow with Neumann BCs. It indicates whether the final state of this flow is turbulent or laminar, that is, whether or not the intermittency boundary at $\text{Re}_L \approx O(100)$ will be reached (for large Re). In other configurations, SC separates the weakly stratified regime in which the buoyancy flux increases with increasing stratification from the strongly stratified regime in which the opposite is observed. In the flux-driven plane channel flow (Nieuwstadt 2005; Flores and Riley 2011; Donda et al. 2015) or Ekman flow (Gohari and Sarkar 2017), the flow may only collapse temporarily, and SC_C could be used to anticipate this temporary collapse (Donda et al. 2015).

- The gradient Richardson number Ri characterizes mixing in the weakly stratified flow (Komori et al. 1983) in a statistically steady state. At each vertical level, it also appears to appropriately characterize the maximum buoyancy flux, which at $z = h$ occurs around Ri = 0.1. Although in a broad sense, turbulence is suppressed more at larger Ri, the mixing is no longer appropriately characterized by Ri in a strongly stratified flow. As such, the collapse of turbulence cannot be associated with a single value of Ri in a wall-bounded flow, consistent with the argument of Shih et al. (2005).

Thus, SC_C describes the mechanism leading to the eventual collapse, not the mechanism of the collapse itself. The value of Re_L at the flux maximum depends on the bulk Reynolds number, which also means that for larger Re, it takes longer for the flow to laminarize after the maximum was reached (e.g., Fig. 13). Finally, the gradient Richardson number appears as a height-dependent and Re-independent parameter to characterize the occurrence of the maximum buoyancy flux. We note that all three of these parameters (Re_L, SC_C, Ri) may be used to discriminate between stability regimes. While this appears unproblematic well within either weak or strong stability, our analysis demonstrates that close to the transition, the attribution of a case to weak or strong stability may critically depend on both the choice of the parameter and the turbulence scale separation. This leaves the question of how these fundamental results may be extended to the collapse of turbulence in reality. With respect to the actual turbulence collapse, earlier results (van Hooijdonk et al. 2015; Monahan et al. 2015) show that the VSBL and WSBL are better characterized by the shear capacity than by, for example, a Richardson number. As such, the shear

capacity provides insight into the mechanism leading to strongly stratified conditions. With respect to Re_L, Flores and Riley (2011) hypothesized that the Re_L criterion could also be extended to flows over a rough surface based on observational data from the CASES-99 experiment (Poulos et al. 2002). This promising hypothesis requires further investigation since it is based on estimates of the boundary layer height (based on the near-surface wind speed) and the surface roughness. Both of these estimates become questionable under strongly stratified conditions. Nonetheless, the importance of near-wall processes in the critical regime of Re_L (as explored in section 3d) actually supports that in a real SBL roughness plays a major role in the collapse or maintenance of turbulence. Hence, the roughness elements may define the scale separation instead of the Kolmogorov length scale (Ghannam et al. 2018). This speculation is corroborated by the order-of-magnitude agreement between Re_L found in numerical studies at moderate Reynold numbers and the real-world SBL (Flores and Riley 2011). It remains, however, unclear how the production of turbulence (i.e., in the buffer layer in traditional wall unit scaling) scales when normalized with a roughness scale.

b. Similarity between boundary conditions

Wall-bounded turbulent flows under neutral stratification have many characteristics that are independent of the particular flow geometry (Kim et al. 1987; Spalart 1988). In fact, characteristics persist in stable conditions when properly scaled in wall units. This is one reason underlying the success of MOST in both realistic (Monin 1970; Holtslag et al. 2013; Mahrt 2014) and idealized flows (García-Villalba and del Álamo 2011; Donda et al. 2015; Deusebio et al. 2015; van Hooijdonk et al. 2017b; Zhou et al. 2017). Considering this generality, the BC type is likely of limited importance in a steady state, at least on the weakly stratified side of the buoyancy flux maximum and $Re_L \gg O(100)$.

While in equilibrium, differences in the higher-order statistical quantities may not affect the mean-flow properties; in strongly perturbed situations, such differences could play a role, as was suggested by Jensen et al. (2016), for the sunset period. Moreover, important differences in dynamical behavior of the mean flow can arise in a Couette flow, and it is natural to explore these differences in configurations other than the Couette flow as well. Previous studies (e.g., Garg et al. 2000; Flores and Riley 2011; García-Villalba and del Álamo 2011; Donda et al. 2015) support a similar rationale for the plane channel flow: In the case of Dirichlet BCs, an intermittent statistically steady state exists at strong stratification (Deusebio et al. 2015). In the case of Neumann BCs, such a state cannot be steady, since flow acceleration also reduces the bulk gradient.

Gohari and Sarkar (2017) performed a direct comparison using different buoyancy BCs for an Ekman flow. They made the comparison at times when the bulk Richardson number (based on the neutral Ekman-layer depth) of the Neumann case was instantaneously equal to the long-time quasi-steady state of a Dirichlet case. The mean horizontal velocity components showed poor agreement between the two types of boundary conditions. This poor agreement may be explained partially by the significant difference in u_τ. The TKE profiles showed reasonable agreement once normalized with u_τ and only when TKE was strong, which in fact further supports scaling in wall units. When TKE was weak, poor agreement was found, which may be explained by the intermittent, and thus statistically inhomogeneous, character of the flow. It would be interesting to revisit this analysis to compare the BCs systematically when the flow is in a similar quasi-steady state in terms of Re_τ.

While the considerations above raise concerns of caution for transient flow configuration, studies of the equilibrium flow may opt for the buoyancy BC that best suits their purposes. Dynamically, however, crucial differences become apparent even in conceptual configurations. While both Neumann and Dirichlet BCs yield important mechanical insight, neither is necessarily more realistic or more suitable than the other. Therefore, if a realistic nonstationary setup is aimed for, the coupling to a surface energy budget is inevitable.

5. Conclusions

Direct numerical simulations of the stably stratified Couette flow have been performed. We quantified the Reynolds number dependence of the buoyancy flux maximum dependency on the Obukhov–Reynolds number. Findings by van Hooijdonk et al. (2017b) are confirmed on a range of Re and on a larger domain. The results show that in a steady state, most first- and second-order statistical quantities are indistinguishable between a Couette flow with Neumann BCs or with Dirichlet BCs. Dynamically, however, differences become apparent that are consistent with the prediction on the dynamic stability of the flow (Phillips 1972; Posmentier 1977; van de Wiel et al. 2007). In the range $Re \approx 1000$–3500, stronger dependence on Re is observed, but at larger Re, the value of SC_C^{crit} appears to converge to approximately 23. We showed theoretically that convergence of SC_C^{crit} is inconsistent with convergence in terms Re_L. Based on analytical considerations, we showed that the occurrence of a maximum buoyancy flux is not controlled by

wall dynamics but rather that it follows from a global constraint. This is consistent with earlier theoretical predictions for the Couette flow by Caulfield and Kerswell (2001) and van de Wiel et al. (2007). However, consistent with Flores and Riley (2011; and later studies), we find that the collapse of turbulence occurs when $Re_L \approx 100$–200. This means that the global constraint inevitably leads to a collapse of turbulence, which actually occurs because of suppression of near-wall structures.

APPENDIX A

Resolution Overview

Table A1 provides an overview of the resolution for each simulation. The resolution is based on steady-state measurements of u_τ. If the simulation did not reach a steady state, the resolution was estimated using the steady-state values of a run with the same Re and a larger value of SC_C (i.e., less stratified).

APPENDIX B

Comparison to the Ekman Flow

In this paper, we have chosen the Couette flow as the main object of interest for its conceptual simplicity. This conceptual approach necessitates the neglect of important physical mechanisms when considering real atmospheric conditions. A step toward more realistic—but not yet atmospheric—conditions may be made by comparing our results to the statistics of the Ekman flow, thus incorporating the effects of rotation, a pressure gradient, and breaking the vertical symmetry. However, a one-to-one comparison is complicated by several factors, such as nonsteadiness of the Ekman flow. Therefore, we compare the flow statistics in the surface layer only. For this purpose, the budget terms of the TKE are defined as

- Shear production $P_{tke} = \langle u'w' \rangle \partial_z U$,
- Viscous transport $V_{tke} = \nu \partial_z \partial_z \langle u_i'^2 \rangle$,

- Pressure transport $\Pi_{tke}^T = -2\partial_z \langle p'w' \rangle$,
- Turbulent transport $T_{tke} = \partial_z \langle u_i'^2 w' \rangle$,
- Dissipation $\varepsilon_{tke} = -2\nu \langle (\partial_z u_i')^2 \rangle$.

Under neutral stratification, the budget terms of the TKE (Fig. B1a) are independent of Re (for Re > 1600), and they match closely with previous results for the Ekman flow (Ansorge and Mellado 2016). This validates our numerical method and provides a further example of the similarity between wall-bounded turbulent flows. For fixed-height statistics, the level $zu_\tau/\nu = 30$ has been chosen, which is at the lower end of the logarithmic region. Therefore, surface-layer scaling should be valid, while external effects that are not present in the Couette flow are minimal. The comparison in Fig. B1b is an illustrative example of more general applicability of the findings that have been discussed in depth for the Couette flow.

APPENDIX C

Theoretical Considerations

The study of Flores and Riley (2011) and the results of van Hooijdonk et al. (2015, 2017b) suggest different criteria indicating the collapse of turbulence. Flores and Riley (2011) base their criterion on whether turbulence can be sustained by near-wall processes, while in van Hooijdonk et al. (2015), a global constraint on the buoyancy flux is defined. The results of the previous sections provide support for both criteria and that they are applicable to different stages of the collapse.

Here, we aim for a qualitative relation for Re_L as function of Re at the point where $SC_C = SC_C^{crit}$ to investigate theoretically if Re_L and SC_C^{crit} are compatible criteria. Moreover, qualitative analytical insight into the Re dependence of the Re_L–SC_C relation supports the interpretation of the DNS results. First, we estimate the maximum total buoyancy flux $\phi_{b,max}$ at $z = h$ following a similar route as in earlier studies (van de Wiel et al. 2012b; van Hooijdonk et al. 2015; van de Wiel et al. 2017), followed by an estimate of Re_L under the assumption that $\phi_b = \phi_{b,max} = q_w$.

The mean buoyancy evolution at a height z may be described by

$$\partial_t b = -\partial_z \langle b'w' \rangle + \kappa_b \partial_z^2 b. \tag{C1}$$

Next, (C1) is integrated between $z = 0$ and $z = h$ and between $z = h$ and $z = 2h$, resulting in

TABLE A1. Overview of the resolution in wall units for all simulations. Asterisks are as in Table 1.

Run	$\dfrac{\delta_x u_\tau}{\nu}$	$\dfrac{\delta_y u_\tau}{\nu}$	$\dfrac{\delta_z u_\tau}{\nu}$	Run	$\dfrac{\delta_x u_\tau}{\nu}$	$\dfrac{\delta_y u_\tau}{\nu}$	$\dfrac{\delta_z u_\tau}{\nu}$	Run	$\dfrac{\delta_x u_\tau}{\nu}$	$\dfrac{\delta_y u_\tau}{\nu}$	$\dfrac{\delta_z u_\tau}{\nu}$
R10	3.0	3.0	0.9	R25S237	3.7	3.3	1.1	R45S225*	3.9	3.7	1.0
R10S271	2.7	2.7	0.8	R25S231*	3.7	3.3	1.1	R45S220**	3.9	3.7	1.0
R10S252	2.5	2.5	0.7	R25S225*	3.7	3.3	1.1				
R10S244*	2.5	2.5	0.7	R25S220*	3.7	3.3	1.1	R62	5.4	5.4	1.3
R10S237*	2.5	2.5	0.7					R62S317	5.0	5.0	1.2
				R35	4.8	4.4	1.4	R62S237	4.3	4.3	1.1
R16	3.5	3.5	1.0	R35S317	4.6	4.2	1.3	R62S231*	4.3	4.3	1.1
R16S317	3.4	3.4	1.0	R35S271	4.4	4.0	1.3	R62S225**	4.3	4.3	1.1
R16S252	3.1	3.1	0.9	R35S237	4.0	3.6	1.2	R62S215*	4.3	4.3	1.1
R16S244	3.0	3.0	0.9	R35S231*	4.0	3.6	1.2				
R16S237*	3.0	3.0	0.9	R35S225*	4.0	3.6	1.2	R16R009	3.4	3.4	1.0
R16S231*	3.0	3.0	0.9	R35S220*	4.0	3.6	1.2	R16R020	3.1	3.1	0.9
R16S225*	3.0	3.0	0.9	R35S215*	4.0	3.6	1.2	R25R010	4.3	3.8	1.3
R16S220*	3.0	3.0	0.9	R35S215*	4.0	3.6	1.2	R25R032	3.7	3.3	1.1
								R35R011	4.6	4.2	1.3
R25	4.5	4.0	1.3	R45	4.8	4.5	1.2	R35R037	4.0	3.6	1.2
R25S317	4.3	3.8	1.3	R45S317	4.5	4.2	1.1	R35VS285	4.0	3.6	1.2
R25S271	4.2	3.7	1.2	R45S237	3.9	3.7	1.0	R35VS237	4.0	3.6	1.2
				R45S231*	3.9	3.7	1.0				

$$\partial_t \mathscr{B}_\downarrow = -\frac{1}{h}\int_0^h \partial_z \langle b'w' \rangle \, dz + \frac{1}{h}\int_0^h \kappa_b \partial_z^2 b \, dz, \quad \text{(C2)}$$

$$\partial_t \mathscr{B}_\uparrow = -\frac{1}{h}\int_h^{2h} \partial_z \langle b'w' \rangle \, dz + \frac{1}{h}\int_h^{2h} \kappa_b \partial_z^2 b \, dz, \quad \text{(C3)}$$

in which $\mathscr{B}_\downarrow = \int_0^h b \, dz/h$ and $\mathscr{B}_\uparrow = \int_h^{2h} b \, dz/h$. Continuing with the integrated buoyancy has the advantage that we do not need to treat the wall processes explicitly using a wall model; that is, we do not assume a specific shape of the velocity and buoyancy profiles.

Combining (C2) with the BCs ($\langle b'w' \rangle = 0$ and $\kappa_b \partial_z b = -q_w$ at the walls) leads to,

$$\partial_t \Delta \mathscr{B} \equiv \partial_t (\mathscr{B}_\uparrow - \mathscr{B}_\downarrow)/2 = q_w + h^{-1}\langle b'w' \rangle_{z=h} - h^{-1}\kappa_b \partial_z b_{z=h}. \quad \text{(C4)}$$

The fluxes are then modeled in bulk form,

$$\langle b'w' \rangle_{z=h} = -\frac{\mathrm{Re}_\tau^2}{\mathrm{Re}^2} U_0 \Delta \mathscr{B} f(\mathrm{Ri}_\mathscr{B}), \quad \text{(C5)}$$

$$\kappa_b \partial_z b_{z=h} = \kappa_b \Delta \mathscr{B}/h, \quad \text{(C6)}$$

with $f(\mathrm{Ri}_\mathscr{B}) = (1 - \alpha \mathrm{Ri}_\mathscr{B})^2$ the Businger–Dyer flux–profile relations (Businger et al. 1971) and the Richardson number based on the integrated buoyancy difference $\mathrm{Ri}_\mathscr{B} = h\Delta \mathscr{B}/U_0^2$. The final result is only quantitatively sensitive to the specific choice of this function, provided it is a decreasing function of $\mathrm{Ri}_\mathscr{B}$, which decreases faster than $\mathrm{Ri}_\mathscr{B}^{-1}$ (Derbyshire 1999); $\alpha \approx 5$ is a model parameter (Högström 1996).

Equations (C5) and (C6) are then inserted into (C4). Furthermore, (C4) is multiplied by h/U_0^3, and the steady state is assumed to arrive at the final dimensionless model equation

$$\partial_\tau \Delta \mathrm{Ri}_\mathscr{B} = 0 = -\frac{\mathrm{Re}_\tau^2}{\mathrm{Re}^2}\mathrm{Ri}_\mathscr{B} f(\mathrm{Ri}_\mathscr{B}) - \frac{\mathrm{Ri}_\mathscr{B}}{\mathrm{RePr}} + \frac{1}{\mathrm{SC}_C^3}, \quad \text{(C7)}$$

with $\tau = tU_0/h$.

Next, we assume that $\mathrm{SC}_C = \mathrm{SC}_C^{\mathrm{crit}}$, that is, SC_C is such that the sum of the first two rhs terms in (C7) maximize. This maximum may be found by derivation with respect to $\mathrm{Ri}_\mathscr{B}$. Since the mathematical structure of (C7) is very similar to the model equation of van de Wiel et al. [2017, their (2)], we do not repeat all steps here. A small difference with their derivation is that we do not assume that $\mathrm{Ri}_{\mathscr{B},\max} = 1/(3\alpha)$ independently of Re, where the subscript "max" refers to a quantity that is measured when $\phi_b = \phi_{b,\max}$. The result is

$$\mathrm{Ri}_{\mathscr{B},\max} = \frac{2}{3\alpha} - \frac{1}{3\alpha}\mathscr{W}, \quad \text{(C8)}$$

with $\mathscr{W} = \sqrt{1 - 3\mathrm{RePr}^{-1}\mathrm{Re}_\tau^{-2}}$. Next, we estimate the relation between Re and Re_τ using a logarithmic profile; that is, $\mathrm{Re} \sim \mathrm{Re}_\tau \ln(\mathrm{Re}_\tau)$ (Townsend 1976). This then leads to

$$\mathrm{Re}/\mathrm{Re}_\tau^2 \sim \mathrm{Re}_\tau \ln(\mathrm{Re}_\tau)/\mathrm{Re}_\tau^2, \quad \text{(C9)}$$

which tends to 0 for $\mathrm{Re} \to \infty$. Consequently, we recover the solution $\mathrm{Ri}_{\mathscr{B},\max} \to 1/(3\alpha)$ of van de Wiel et al. (2007) when $\mathrm{Re} \to \infty$. The corresponding maximum buoyancy flux is
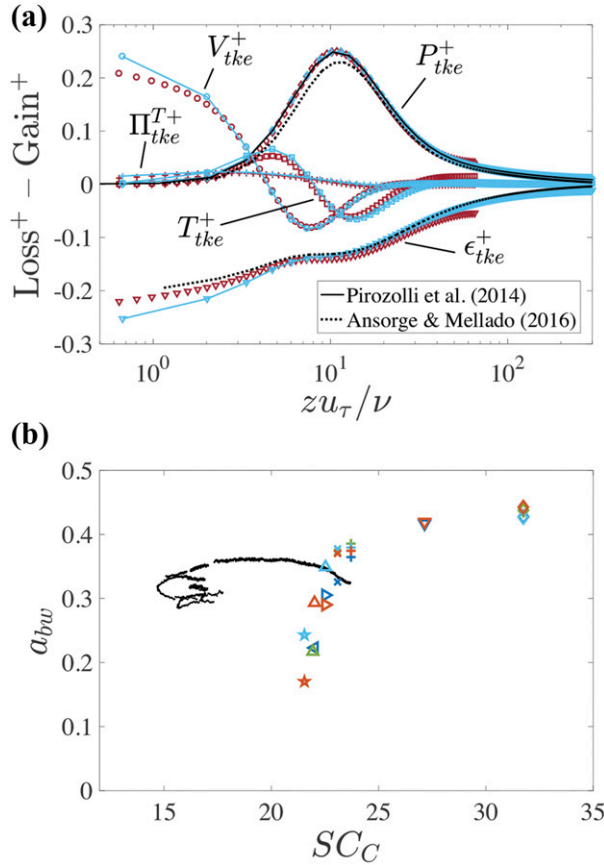
FIG. B1. (a) Profiles of the TKE budget terms. Only results for Re = 1600 (red) and Re = 6200 (blue) are shown for clarity (for other Re, the results are virtually the same). The various terms are indicated in the figure. The solid black line represents results for the Couette flow at RE = 21 333 obtained by Pirozzoli et al. (2014, production term only). The dotted black lines indicate results for the Ekman flow obtained by (Ansorge and Mellado 2016, production and dissipation term). (b) Values at the end of each simulation, where the symbols indicate SC_C: 31.7 ($\diamond$), 27.1 ($\triangledown$), 25.2 (*), 24.4 ($\bigcirc$), 23.7 (+), 23.1 ($\times$), 22.5 ($\triangleright$), 22.0 ($\triangle$), and 21.5 ($\star$). Black dots indicate the results for the Ekman flow, with SC_C based on the geostrophic wind speed and an estimate of the boundary layer depth. Note that these data may be arbitrarily shifted within an order of magnitude by using different definitions of the boundary layer depth.

$$\hat{\phi}_{b,\max} = \frac{2 - \mathscr{W}}{27\alpha}\left[\frac{9}{\mathrm{PrRe}} + \frac{\mathrm{Re}_\tau^2}{\mathrm{Re}^2}(1 + \mathscr{W})^2\right]. \quad (C10)$$

Again, when Re → ∞, the result of van de Wiel et al. (2017, and earlier papers) is retrieved:

$$\lim_{\mathrm{Re}\to\infty} \hat{\phi}_{b,\max} = \frac{4\mathrm{Re}_\tau^2}{27\alpha\mathrm{Re}^2}. \quad (C11)$$

Finally, we may use (C10) and (5) to estimate $\mathrm{Re}_L = \mathrm{Re}_\tau^4 \mathrm{Re}^{-3} \hat{\phi}_{b,\max}^{-1}$,

$$\mathrm{Re}_L = \frac{1}{\kappa}\frac{\mathrm{Re}_\tau^4}{\mathrm{Re}^3}\frac{27\alpha}{(2 - \mathscr{W})\left[\dfrac{9}{\mathrm{PrRe}} + \dfrac{\mathrm{Re}_\tau^2}{\mathrm{Re}^2}(1 + \mathscr{W})^2\right]}, \quad (C12)$$

and

$$\lim_{\mathrm{Re}\to\infty} \mathrm{Re}_L = \frac{27\alpha\mathrm{Re}_\tau^2}{4\kappa\mathrm{Re}}. \quad (C13)$$

Using (C9), this results in

$$\mathrm{Re}_L \sim \frac{27\alpha}{4\kappa}\frac{\mathrm{Re}_\tau}{\ln(\mathrm{Re}_\tau)}. \quad (C14)$$

REFERENCES

André, J. C., and L. Mahrt, 1982: The nocturnal surface inversion and influence of clear-air radiative cooling. *J. Atmos. Sci.*, **39**, 864–878, https://doi.org/10.1175/1520-0469(1982)039<0864:TNSIAI>2.0.CO;2.

Ansorge, C., 2017: *Analyses of Turbulence in the Neutrally and Stably Stratified Planetary Boundary Layer.* Springer, 171 pp.

——, and J. P. Mellado, 2014: Global intermittency and collapsing turbulence in the stratified planetary boundary layer. *Bound.-Layer Meteor.*, **153**, 89–116, https://doi.org/10.1007/s10546-014-9941-3.

——, and ——, 2016: Analyses of external and global intermittency in the logarithmic layer of Ekman flow. *J. Fluid Mech.*, **805**, 611–635, https://doi.org/10.1017/jfm.2016.534.

Armenio, V., and S. Sarkar, 2002: An investigation of stably stratified turbulent channel flow using large-eddy simulation. *J. Fluid Mech.*, **459**, 1–42, https://doi.org/10.1017/S0022112002007851.

Bartello, P., and S. M. Tobias, 2013: Sensitivity of stratified turbulence to the buoyancy Reynolds number. *J. Fluid Mech.*, **725**, 1–22, https://doi.org/10.1017/jfm.2013.170.

Basu, S., A. A. M. Holtslag, B. J. H. van de Wiel, A. F. Moene, and G.-J. Steeneveld, 2008: An inconvenient "truth" about using sensible heat flux as a surface boundary condition in models under stably stratified regimes. *Acta Geophys.*, **56**, 88–99, https://doi.org/10.2478/s11600-007-0038-y.

Billant, P., and J.-M. Chomaz, 2001: Self-similarity of strongly stratified inviscid flows. *Phys. Fluids*, **13**, 1645–1651, https://doi.org/10.1063/1.1369125.

Brethouwer, G., P. Billant, E. Lindborg, and J.-M. Chomaz, 2007: Scaling analysis and simulation of strongly stratified turbulent flows. *J. Fluid Mech.*, **585**, 343–368, https://doi.org/10.1017/S0022112007006854.

Businger, J. A., 1973: Turbulent transfer in the atmospheric surface layer. *Workshop on Micrometeorology*, D. A. Haugen, Ed., Amer. Meteor. Soc., 67–98.

——, J. C. Wyngaard, Y. Izumi, and E. F. Bradley, 1971: Flux-profile relationships in the atmospheric surface layer. *J. Atmos. Sci.*, **28**, 181–189, https://doi.org/10.1175/1520-0469(1971)028<0181:FPRITA>2.0.CO;2.

Caulfield, C. P., and R. R. Kerswell, 2001: Maximal mixing rate in turbulent stably stratified Couette flow. *Phys. Fluids*, **13**, 894–900, https://doi.org/10.1063/1.1351856.

Derbyshire, S. H., 1999: Boundary-layer decoupling over cold surfaces as a physical boundary-instability. *Bound.-Layer Meteor.*, **90**, 297–325, https://doi.org/10.1023/A:1001710014316.

Deusebio, E., C. P. Caulfield, and J. R. Taylor, 2015: The intermittency boundary in stratified plane Couette flow. *J. Fluid Mech.*, **781**, 298–329, https://doi.org/10.1017/jfm.2015.497.

Donda, J. M. M., I. G. S. van Hooijdonk, A. F. Moene, H. J. J. Jonker, G. J. F. van Heijst, H. J. H. Clercx, and B. J. H. van de Wiel, 2015: Collapse of turbulence in stably stratified channel flow: A transient phenomenon. *Quart. J. Roy. Meteor. Soc.*, **141**, 2137–2147, https://doi.org/10.1002/qj.2511.

Fedorovich, E., J. A. Gibbs, and A. Shapiro, 2017: Numerical study of nocturnal low-level jets over gently sloping terrain. *J. Atmos. Sci.*, **74**, 2813–2834, https://doi.org/10.1175/JAS-D-17-0013.1.

Fernando, H. J. S., and J. C. Weil, 2010: Whither the stable boundary layer? *Bull. Amer. Meteor. Soc.*, **91**, 1475–1484, https://doi.org/10.1175/2010BAMS2770.1.

Flores, O., and J. J. Riley, 2011: Analysis of turbulence collapse in the stably stratified surface layer using direct numerical simulation. *Bound.-Layer Meteor.*, **139**, 241–259, https://doi.org/10.1007/s10546-011-9588-2.

Fritts, D. C., L. Wang, M. A. Geller, D. A. Lawrence, J. Werne, and B. B. Balsley, 2016: Numerical modeling of multiscale dynamics at a high Reynolds number: Instabilities, turbulence, and an assessment of Ozmidov and Thorpe scales. *J. Atmos. Sci.*, **73**, 555–578, https://doi.org/10.1175/JAS-D-14-0343.1.

García-Villalba, M., and J. C. del Álamo, 2011: Turbulence modification by stable stratification in channel flow. *Phys. Fluids*, **23**, 045104, https://doi.org/10.1063/1.3560359.

Garg, R. P., J. H. Ferziger, S. G. Monismith, and J. R. Koseff, 2000: Stably stratified turbulent channel flows. I. Stratification regimes and turbulence suppression mechanism. *Phys. Fluids*, **12**, 2569–2594, https://doi.org/10.1063/1.1288608.

Ghannam, K., G. G. Katul, E. Bou-Zeid, T. Gerken, and M. Chamecki, 2018: Scaling and similarity of the anisotropic coherent eddies in near-surface atmospheric turbulence. *J. Atmos. Sci.*, **75**, 943–964, https://doi.org/10.1175/JAS-D-17-0246.1.

Gibbs, J. A., E. Fedorovich, and A. Shapiro, 2015: Revisiting surface heat-flux and temperature boundary conditions in models of stably stratified boundary-layer flows. *Bound.-Layer Meteor.*, **154**, 171–187, https://doi.org/10.1007/s10546-014-9970-y.

Gohari, S. M. I., and S. Sarkar, 2017: Direct numerical simulation of turbulence collapse and rebirth in stably stratified Ekman flow. *Bound.-Layer Meteor.*, **162**, 401–426, https://doi.org/10.1007/s10546-016-0206-1.

Grachev, A. A., E. L Andreas, C. W. Fairall, P. S. Guest, and P. O. G. Persson, 2013: The critical Richardson number and limits of applicability of local similarity theory in the stable boundary layer. *Bound.-Layer Meteor.*, **147**, 51–82, https://doi.org/10.1007/s10546-012-9771-0.

Högström, U., 1996: Review of some basic characteristics of the atmospheric surface layer. *Bound.-Layer Meteor.*, **78**, 215–246, https://doi.org/10.1007/BF00120937.

Holdsworth, A. M., T. Rees, and A. H. Monahan, 2016: Parameterization sensitivity and instability characteristics of the maximum sustainable heat flux framework for predicting turbulent collapse. *J. Atmos. Sci.*, **73**, 3527–3540, https://doi.org/10.1175/JAS-D-16-0057.1.

Holford, J. M., and P. F. Linden, 1999: Turbulent mixing in a stratified fluid. *Dyn. Atmos. Oceans*, **30**, 173–198, https://doi.org/10.1016/S0377-0265(99)00025-1.

Holtslag, A. A. M., and Coauthors, 2013: Stable atmospheric boundary layers and diurnal cycles: Challenges for weather and climate models. *Bull. Amer. Meteor. Soc.*, **94**, 1691–1706, https://doi.org/10.1175/BAMS-D-11-00187.1.

Jacobitz, F. G., S. Sarkar, and C. W. Van Atta, 1997: Direct numerical simulations of the turbulence evolution in a uniformly sheared and stably stratified flow. *J. Fluid Mech.*, **342**, 231–261, https://doi.org/10.1017/S0022112097005478.

Jensen, D. D., D. F. Nadeau, S. W. Hoch, and E. R. Pardyjak, 2016: Observations of near-surface heat-flux and temperature profiles through the early evening transition over contrasting surfaces. *Bound.-Layer Meteor.*, **159**, 567–587, https://doi.org/10.1007/s10546-015-0067-z.

Kim, J., and P. Moin, 1985: Application of a fractional-step method to incompressible Navier-Stokes equations. *J. Comput. Phys.*, **59**, 308–323, https://doi.org/10.1016/0021-9991(85)90148-2.

——, ——, and R. Moser, 1987: Turbulence statistics in fully developed channel flow at low Reynolds number. *J. Fluid Mech.*, **177**, 133–166, https://doi.org/10.1017/S0022112087000892.

Komori, S., H. Ueda, F. Ogino, and T. Mizushina, 1983: Turbulence structure in stably stratified open-channel flow. *J. Fluid Mech.*, **130**, 13–26, https://doi.org/10.1017/S0022112083000944.

Linden, P. F., 1979: Mixing in stratified fluids. *Geophys. Astrophys. Fluid Dyn.*, **13**, 3–23, https://doi.org/10.1080/03091927908243758.

Mahrt, L., 2014: Stably stratified atmospheric boundary layers. *Annu. Rev. Fluid Mech.*, **46**, 23–45, https://doi.org/10.1146/annurev-fluid-010313-141354.

——, J. Sun, W. Blumen, T. Delany, and S. Oncley, 1998: Nocturnal boundary-layer regimes. *Bound.-Layer Meteor.*, **88**, 255–278, https://doi.org/10.1023/A:1001171313493.

Malhi, Y. S., 1995: The significance of the dual solutions for heat fluxes measured by the temperature fluctuation method in stable conditions. *Bound.-Layer Meteor.*, **74**, 389–396, https://doi.org/10.1007/BF00712379.

Marlatt, S., S. Waggy, and S. Biringen, 2012: Direct numerical simulation of the turbulent Ekman layer: Evaluation of closure models. *J. Atmos. Sci.*, **69**, 1106–1117, https://doi.org/10.1175/JAS-D-11-0107.1.

Mauritsen, T., G. Svensson, S. S. Zilitinkevich, I. Esau, L. Enger, and B. Grisogono, 2007: A total turbulent energy closure model for neutrally and stably stratified atmospheric boundary layers. *J. Atmos. Sci.*, **64**, 4113–4126, https://doi.org/10.1175/2007JAS2294.1.

McNider, R. T., D. E. England, M. J. Friedman, and X. Shi, 1995: Predictability of the stable atmospheric boundary layer. *J. Atmos. Sci.*, **52**, 1602–1614, https://doi.org/10.1175/1520-0469(1995)052<1602:POTSAB>2.0.CO;2.

Mellado, J. P., 2012: Direct numerical simulation of free convection over a heated plate. *J. Fluid Mech.*, **712**, 418–450, https://doi.org/10.1017/jfm.2012.428.

Moin, P., and K. Mahesh, 1998: Direct numerical simulation: A tool in turbulence research. *Annu. Rev. Fluid Mech.*, **30**, 539–578, https://doi.org/10.1146/annurev.fluid.30.1.539.

Monahan, A. H., T. Rees, Y. He, and N. McFarlane, 2015: Multiple regimes of wind, stratification, and turbulence in the stable boundary layer. *J. Atmos. Sci.*, **72**, 3178–3198, https://doi.org/10.1175/JAS-D-14-0311.1.

Monin, A. S., 1970: The atmospheric boundary layer. *Annu. Rev. Fluid Mech.*, **2**, 225–250, https://doi.org/10.1146/annurev.fl.02.010170.001301.

Nadeau, D. F., E. R. Pardyjak, C. W. Higgins, H. J. S. Fernando, and M. B. Parlange, 2011: A simple model for the afternoon and early evening decay of convective turbulence over different land surfaces. *Bound.-Layer Meteor.*, **141**, 301–324, https://doi.org/10.1007/s10546-011-9645-x.

Nieuwstadt, F. T. M., 2005: Direct numerical simulation of stable channel flow at large stability. *Bound.-Layer Meteor.*, **116**, 277–299, https://doi.org/10.1007/s10546-004-2818-0.

Phillips, O. M., 1972: Turbulence in a strongly stratified fluid—Is it unstable? *Deep-Sea Res. Oceanogr. Abstr.*, **19**, 79–81, https://doi.org/10.1016/0011-7471(72)90074-5.

Pirozzoli, S., M. Bernardini, and P. Orlandi, 2014: Turbulence statistics in Couette flow at high Reynolds number. *J. Fluid Mech.*, **758**, 327–343, https://doi.org/10.1017/jfm.2014.529.

Posmentier, E. S., 1977: The generation of salinity finestructure by vertical diffusion. *J. Phys. Oceanogr.*, **7**, 298–300, https://doi.org/10.1175/1520-0485(1977)007<0298:TGOSFB>2.0.CO;2.

Poulos, G. S., and Coauthors, 2002: CASES-99: A comprehensive investigation of the stable nocturnal boundary layer. *Bull. Amer. Meteor. Soc.*, **83**, 555–581, https://doi.org/10.1175/1520-0477(2002)083<0555:CACIOT>2.3.CO;2.

Scotti, A., and B. White, 2016: The mixing efficiency of stratified turbulent boundary layers. *J. Phys. Oceanogr.*, **46**, 3181–3191, https://doi.org/10.1175/JPO-D-16-0095.1.

Shah, S. K., and E. Bou-Zeid, 2014: Direct numerical simulations of turbulent Ekman layers with increasing static stability: Modifications to the bulk structure and second-order statistics. *J. Fluid Mech.*, **760**, 494–539, https://doi.org/10.1017/jfm.2014.597.

Shih, L. H., J. R. Koseff, G. N. Ivey, and J. H. Ferziger, 2005: Parameterization of turbulent fluxes and scales using homogeneous sheared stably stratified turbulence simulations. *J. Fluid Mech.*, **525**, 193–214, https://doi.org/10.1017/S0022112004002587.

Smirnova, T. G., J. M. Brown, and S. G. Benjamin, 1997: Performance of different soil model configurations in simulating ground surface temperature and surface fluxes. *Mon. Wea. Rev.*, **125**, 1870–1884, https://doi.org/10.1175/1520-0493(1997)125<1870:PODSMC>2.0.CO;2.

Smyth, W. D., and J. N. Moum, 2000: Anisotropy of turbulence in stably stratified mixing layers. *Phys. Fluids*, **12**, 1343–1362, https://doi.org/10.1063/1.870386.

Spalart, P. R., 1988: Direct simulation of a turbulent boundary layer up to $R_\theta = 1410$. *J. Fluid Mech.*, **187**, 61–98, https://doi.org/10.1017/S0022112088000345.

Steeneveld, G. J., B. J. H. van de Wiel, and A. A. M. Holtslag, 2006: Modeling the evolution of the atmospheric boundary layer coupled to the land surface for three contrasting nights in CASES-99. *J. Atmos. Sci.*, **63**, 920–935, https://doi.org/10.1175/JAS3654.1.

Sun, J., and Coauthors, 2015: Review of wave-turbulence interactions in the stable atmospheric boundary layer. *Rev. Geophys.*, **53**, 956–993, https://doi.org/10.1002/2015RG000487.

Taylor, P. A., 1971: A note on the log-linear velocity profile in stable conditions. *Quart. J. Roy. Meteor. Soc.*, **97**, 326–329, https://doi.org/10.1002/qj.49709741308.

Townsend, A. A., 1976: *The Structure of Turbulent Shear Flow*. Cambridge University Press, 438 pp.

van de Wiel, B. J. H., A. F. Moene, G. J. Steeneveld, O. K. Hartogensis, and A. A. M. Holtslag, 2007: Predicting the collapse of turbulence in stably stratified boundary layers. *Flow Turbul. Combust.*, **79**, 251–274, https://doi.org/10.1007/s10494-007-9094-2.

——, ——, and H. J. J. Jonker, 2012a: The cessation of continuous turbulence as precursor of the very stable nocturnal boundary layer. *J. Atmos. Sci.*, **69**, 3097–3115, https://doi.org/10.1175/JAS-D-12-064.1.

——, ——, ——, P. Baas, S. Basu, J. M. M. Donda, J. Sun, and A. A. M. Holtslag, 2012b: The minimum wind speed for sustainable turbulence in the nocturnal boundary layer. *J. Atmos. Sci.*, **69**, 3116–3127, https://doi.org/10.1175/JAS-D-12-0107.1.

——, and Coauthors, 2017: Regime transitions in near-surface temperature inversions: A conceptual model. *J. Atmos. Sci.*, **74**, 1057–1073, https://doi.org/10.1175/JAS-D-16-0180.1.

van Driest, E. R., 1956: On turbulent flow near a wall. *J. Aeronaut. Sci.*, **23**, 1007–1011, https://doi.org/10.2514/8.3713.

van Heerwaarden, C. C., and J. P. Mellado, 2016: Growth and decay of a convective boundary layer over a surface with a constant temperature. *J. Atmos. Sci.*, **73**, 2165–2177, https://doi.org/10.1175/JAS-D-15-0315.1.

——, B. J. van Stratum, T. Heus, J. A. Gibbs, E. Fedorovich, and J. P. Mellado, 2017: MicroHH 1.0: A computational fluid dynamics code for direct numerical simulation and large-eddy simulation of atmospheric boundary layer flows. *Geosci. Model Dev.*, **10**, 3145–3165, https://doi.org/10.5194/gmd-10-3145-2017.

van Hooijdonk, I. G. S., J. M. M. Donda, H. J. H. Clercx, F. C. Bosveld, and B. J. H. van de Wiel, 2015: Shear capacity as prognostic for nocturnal boundary layer regimes. *J. Atmos. Sci.*, **72**, 1518–1532, https://doi.org/10.1175/JAS-D-14-0140.1.

——, and Coauthors, 2017a: Near-surface temperature inversion growth rate during the onset of the stable boundary layer. *J. Atmos. Sci.*, **74**, 3433–3449, https://doi.org/10.1175/JAS-D-17-0084.1.

——, A. F. Moene, M. Scheffer, H. J. H. Clercx, and B. J. H. van de Wiel, 2017b: Early warning signals for regime transition in the stable boundary layer: A model study. *Bound.-Layer Meteor.*, **162**, 283–306, https://doi.org/10.1007/s10546-016-0199-9.

Vignon, E., and Coauthors, 2017: Stable boundary-layer regimes at Dome C, Antarctica: Observation and analysis. *Quart. J. Roy. Meteor. Soc.*, **143**, 1241–1253, https://doi.org/10.1002/qj.2998.

Wilson, J. M., and S. K. Venayagamoorthy, 2015: A shear-based parameterization of turbulent mixing in the stable atmospheric boundary layer. *J. Atmos. Sci.*, **72**, 1713–1726, https://doi.org/10.1175/JAS-D-14-0241.1.

Zhou, Q., J. R. Taylor, and C. P. Caulfield, 2017: Self-similar mixing in stratified plane Couette flow for varying Prandtl number. *J. Fluid Mech.*, **820**, 86–120, https://doi.org/10.1017/jfm.2017.200.